Available online at www.sciencedirect.com

ScienceDirect

Geochimica et Cosmochimica Acta 214 (2017) 86–114

Geochimica et Cosmochimica Acta

www.elsevier.com/locate/gca

Chemical and physical changes during seawater flow through intact dunite cores: An experimental study at 150–200 °C

Andrew J. Luhmann [a,b,*], Benjamin M. Tutolo [b,c], Brian C. Bagley [b], David F.R. Mildner [d], Peter P. Scheuermann [b], Joshua M. Feinberg [b,e], Konstantin Ignatyev [f], William E. Seyfried Jr. [b]

[a] Department of Earth and Environmental Science, New Mexico Institute of Mining and Technology, 801 Leroy Place, Socorro, NM 87801, USA
[b] Department of Earth Sciences, University of Minnesota, 310 Pillsbury Drive SE, Minneapolis, MN 55455, USA
[c] Department of Earth Sciences, University of Oxford, South Parks Road, Oxford OX1 3AN, UK
[d] NIST Center for Neutron Research, National Institute of Standards and Technology, Gaithersburg, MD 20899, USA
[e] Institute for Rock Magnetism, University of Minnesota, 100 Union Street SE, Minneapolis, MN 55455, USA
[f] Diamond Light Source, Harwell Campus, Didcot OX11 0DE, UK

Received 23 December 2016; accepted in revised form 11 July 2017; available online 19 July 2017

Abstract

Two flow-through experiments were conducted to assess serpentinization of intact dunite cores. Permeability and fluid chemistry indicate significantly more reaction during the second experiment at 200 °C than the first experiment at 150 °C. Permeability decreased by a factor of 2.4 and 25 during the experiments at 150 and 200 °C, respectively. Furthermore, hydrogen and methane concentrations exceeded 600 μmol/kg and 300 μmol/kg during the 200 °C experiment, and were one and two orders of magnitude higher, respectively, than the 150 °C experiment. Fe K-edge X-ray absorption near edge structure analyses of alteration minerals demonstrated Fe oxidation that occurred during the 200 °C experiment. Vibrating sample magnetometer measurements on post-experimental cores indicated little to no magnetite production, suggesting that the hydrogen was largely generated by the oxidation of iron as olivine was converted to ferric iron (Fe(III)) serpentine and/or saponite. Scanning electron microscopy images suggested secondary mineralization on the post-experimental core from the 200 °C experiment, portraying the formation of a secondary phase with a honeycomb-like texture as well as calcite and wollastonite. Scanning electron microscopy images also illustrated dissolution along linear bands through the interiors of olivine crystals, possibly along pathways with abundant fluid inclusions. Energy dispersive X-ray spectroscopy identified Cl uptake in serpentine, while Fourier transform-infrared spectroscopy suggested the formation of serpentine, saponite, and talc. However, no change was observed when comparing pre- and post-experimental X-ray computed tomography scans of the cores. Furthermore, (ultra) small angle neutron scattering datasets were collected to assess changes in porosity, surface area, and fractal characteristics of the samples over the ≈ 1 nm- to 10 μm-scale range. The results from the 200 °C post-experimental core generally fell within the range of values for the two pristine samples and the 150 °C post-experimental core that underwent negligible reaction, indicating that any change from reaction was smaller than the natural variability of the dunite. Even though there was little physical evidence of alteration, the initial stage of serpentinization at 200 °C was sufficiently significant to have a dramatic effect on flow fields in the core. Furthermore, this experiment generated significant dissolved hydrogen concentrations while simulating open system dynamics. Even though open systems prevent elevated hydrogen concentrations due to continual loss of hydrogen, we speculate that this process is responsible for stabilizing ferric Fe-rich serpentine in nature while

* Corresponding author at: Department of Earth and Environmental Science, New Mexico Institute of Mining and Technology, 801 Leroy Place, Socorro, NM 87801, USA. Tel.: +1 575 835 5029.
E-mail address: andrew.luhmann@nmt.edu (A.J. Luhmann).

http://dx.doi.org/10.1016/j.gca.2017.07.020

also oxidizing more ferrous iron (Fe(II)) and cumulatively generating more hydrogen than would be possible in a closed system.

Keywords: Serpentinization; Hydrogen; Permeability; Fluid-rock interaction; Lost City; (Ultra) small angle neutron scattering ((U)SANS); X-ray computed tomography (XRCT); Vibrating sample magnetometer (VSM); Fourier transform-infrared (FT-IR) spectroscopy; X-ray absorption near edge structure (XANES) spectroscopy

1. INTRODUCTION

Peridotites, olivine-rich rocks originating in the mantle, are commonly exposed at slow-spreading ridges and subduction zones due to tectonic processes (Guillot and Hattori, 2013). Once near the surface, serpentinization then proceeds and involves the hydration of peridotite at relatively low temperatures (McCollom and Bach, 2009; Klein et al., 2013) during interaction between groundwater/seawater and ultramafic rock (Moody, 1976; Nesbitt and Bricker, 1978; Janecky and Seyfried, 1986; O'Hanley, 1996; Schroeder et al., 2002). Experimental studies of serpentinization have demonstrated significant complexity, with reaction kinetics that span ≈ 4 orders of magnitude (Martin and Fyfe, 1970; Wegner and Ernst, 1983; Lafay et al., 2012; Malvoisin et al., 2012b; Andreani et al., 2013a,b; McCollom et al., 2016). Serpentinization has important implications for geochemical cycling due to alteration of ultramafic rocks (Allen and Seyfried, 2003; Bach et al., 2004; Boschi et al., 2006; Seyfried et al., 2007, 2010, 2015; Foustoukos et al., 2008). Furthermore, serpentinization produces fluids that contain hydrogen (H_2) and methane (CH_4) (e.g., Charlou et al., 2002; Kelley et al., 2005), with the potential to support biological communities without photosynthesis (Brazelton et al., 2006; Flores et al., 2011; McCollom and Seewald, 2013). While H_2 is produced from reaction between water and ferrous Fe-rich (Fe(II)) olivine, the generated H_2 can create environments that facilitate abiotic production of CH_4 as CO_2 is reduced (Horita and Berndt, 1999; McCollom and Seewald, 2001; Foustoukos and Seyfried, 2004). Flow-through experimental studies have demonstrated permeability reductions caused by serpentinization reactions that clog flow paths (Godard et al., 2013; Farough et al., 2016). In addition, geophysical implications arise as rock density is dramatically reduced (Toft et al., 1990; O'Hanley, 1996; Oufi et al., 2002; Bach et al., 2006; Beard et al., 2009) and magnetite forms during serpentinization, which significantly changes the magnetic properties of ultramafic rocks (Toft et al., 1990; Oufi et al., 2002; Schroeder et al., 2002; Maffione et al., 2014). Because of the density reduction, serpentinization causes a solid volume expansion, but reaction-driven cracking potentially provides a positive feedback mechanism that maintains or creates flow pathways, ultimately producing rocks that have become fully serpentinized (Macdonald and Fyfe, 1985; Kelemen and Hirth, 2012; Plümper et al., 2012; Tutolo et al., 2016).

Serpentinization in ultramafic-hosted hydrothermal systems can produce relatively cool and alkaline fluids that support diverse ecosystems (Palandri and Reed, 2004; Kelley et al., 2005). The Lost City hydrothermal field, which was discovered in 2001, ≈15 km from the Mid-Atlantic Ridge at 30°N (Kelley et al., 2001, 2005; Früh-Green et al., 2003), provides strong evidence for the feedback between detachment faulting and serpentinization by seawater of exposed mantle lithologies. This site includes vent temperatures up to 90 °C and spectacular carbonate chimneys that rise up to 60 m above the ocean floor (Früh-Green et al., 2003; Kelley et al., 2005). Below the surface, olivine is hydrated to form secondary phases that include serpentine, talc, magnetite, and brucite as serpentinization proceeds (Kelley et al., 2005; Boschi et al., 2006, 2008). Boschi et al. (2006) documented complex heterogeneities of mass transfer during alteration of the Atlantis Massif (oceanic core complex which hosts the Lost City Hydrothermal Field) and noted that seawater-gabbro interaction can be an important source of Si during serpentinization of ultramafic rocks. Similarly, Seyfried et al. (2015) show that Lost City vent fluid chemistries are influenced by rocks bearing considerably more SiO_2 than peridotite alone. Isotopic evidence suggests that the alteration at Lost City has resulted in the abiotic production of hydrocarbons and formate (Proskurowski et al., 2008; Lang et al., 2010).

To simulate the serpentinization of ultramafic rocks, we conducted two flow through experiments on intact dunite cores to document chemical reactions during incipient stages of serpentinization and to identify the effects of these reactions on flow and rock physical properties. Artificial seawater flowed through the dunite cores during the experiments, and the far-from-equilibrium experimental fluid produced a strong thermodynamic drive for reaction. The experimental flow system permitted periodic collection of fluid chemistry to constrain fluid-rock reactions, and simultaneous permeability measurements demonstrated the effect of reactions on flow fields through each core. A variety of analyses were performed on the core samples to document mineralogical and pore changes. The coupling of these datasets informs the understanding of reaction zones in ultramafic hydrothermal systems, with implications for Lost City-type systems.

2. METHODS

Experiments were conducted using a novel flow system (Fig. 1) to mimic physical and chemical processes in serpentinizing systems. Watlow heating bands and Teledyne ISCO syringe pumps facilitate temperature and pressure control of the flow-through reaction cell, and the reaction cell's design enables confinement pressure to be applied equally

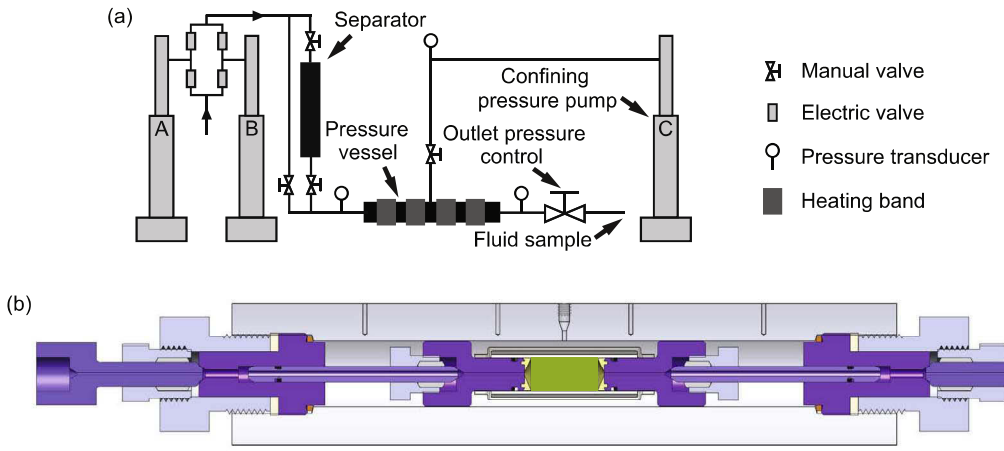

Fig. 1. (a) Hydrothermal flow-through reaction system facilitates dunite-seawater reactions at 150–200 °C and 150 bar pore-fluid pressure, while simultaneously monitoring permeability and fluid chemistry evolution. (b) Fluid-rock reaction occurs in the pressure vessel with many custom-made components (Luhmann et al., 2017a). O-rings on piston assemblies permit confinement pressure to be applied equally in all directions on the experimental core. Experimental fluid only contacts titanium components (colored purple) when at experimental temperature. (For interpretation of the references to color in this figure legend, the reader is referred to the web version of this article.)

along all directions of the (PFA) Teflon-sheathed experimental core. Within the heated pressure vessel, experimental solution flows through titanium (Ti-6Al-4V) flow pieces, which were heated to 500 °C until the surfaces became a bronze to purple color, indicating an oxidized and passivated surface (Fig. 1b). Furthermore, in-situ changes in fluid chemistry and permeability can be monitored simultaneously. Outlet pressure was controlled using a computer-controlled needle valve designed in-house. Thus, the experimental system enables continuous fluid sample collection while maintaining pressure in the flow-through cell. The samples may be analyzed for dissolved solids and gases, which provide detailed characterization of mass transfer that occurs in the reacted core, while continuous permeability measurements indicate the impact of the reactions on fluid flow through the sample in real time. Furthermore, the experimental core can be analyzed after the experiment for mineralogical and porosity changes. The flow system has been employed in a series of experiments (Luhmann et al., 2013, 2014; Tutolo et al., 2014, 2015), and the reaction cell is described in more detail in Luhmann et al. (2017a).

Our experiments were conducted on solid cores (1.26 cm in diameter by 2.62–2.68 cm long) cut from a hand sample of Balsam Gap Dunite from North Carolina. The dunite composition (with 2σ accuracies better than 3%) was determined by inductively coupled plasma-optical emission spectrometry (ICP-OES) (Table 1). Petrographic analyses indicate olivine, with minor orthopyroxene, clinopyroxene, plagioclase, and chromite (Fig. 2). Olivine grains within the core sample generally range from ≈100 μm to 1 mm in size and are surrounded by incipient serpentinization phases, likely primarily serpentine (Table 5), as evidenced by unique birefringence at grain boundaries. Orthopyroxenes display minor deformation, and concentrations of ortho- and clinopyroxene show localized alteration to fine-grained oxides and phyllosilicates. Furthermore, rare muscovite, amphibole, and other mineral phases cannot

Table 1
Chemical composition of Balsam Gap Dunite.

Oxide	wt%
Al_2O_3	0.21
BaO	<DL
CaO	0.108
FeO	7.3
K_2O	0.0239
MgO	50
MnO	0.112
Na_2O	0.021
P_2O_5	<DL
SiO_2	43
SrO	0.00137
TiO_2	0.0049
Total	101

DL = detection limit.

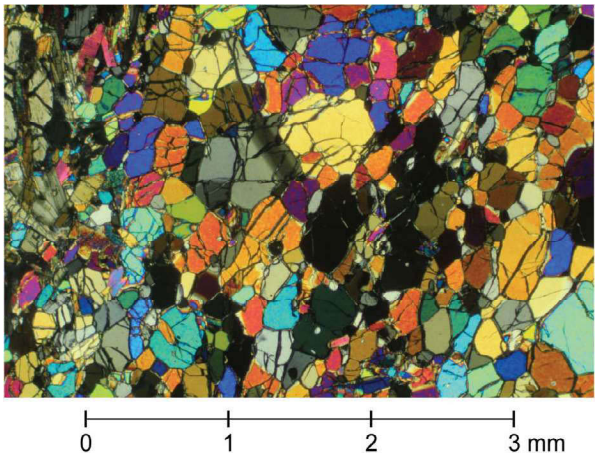

Fig. 2. Cross-polarized light micrograph of dunite sample with relatively fresh olivine and little alteration. Other mineral phases are minor.

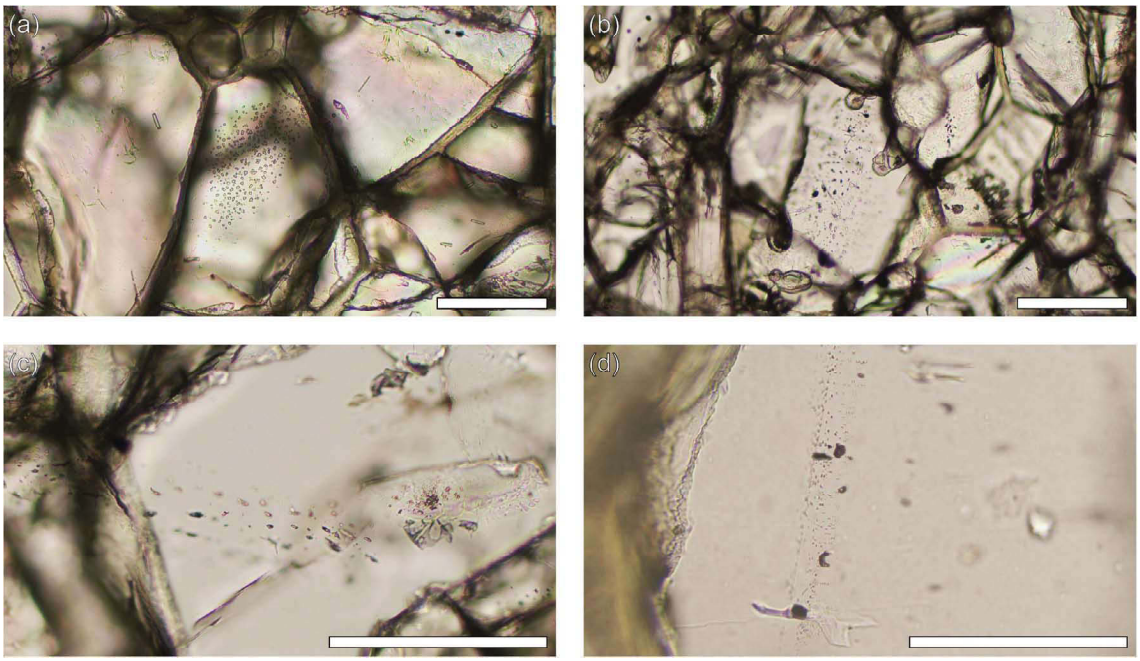

Fig. 3. Plane-polarized light micrographs illustrating fluid inclusions in crystals within the dunite sample. The distribution of fluid inclusions ranges from (a) random to (b) sub-linear bands to (c and d) linear streaks. The sections are 150 μm thick, and a video is included in the Supplementary Material that better illustrates the bands of fluid inclusions with depth with one of the crystals shown in (b). Previous research has also noted linear bands of fluid inclusions along growth planes (Liu and Fei, 2006). Each micrograph includes a 100 μm scale bar.

be ruled out. Calculation of normative mineralogy (using the data provided in Table 1) suggests the sample includes 93.2 wt% olivine, 6.12 wt% ferroan enstatite, 0.59 wt% magnetite, and 0.43 wt% diopside,[1] although chromite was not quantified due to the lack of a Cr analysis (Table 1) and vibrating sample magnetometer analyses indicate negligible magnetite (Table 7). Energy dispersive X-ray spectroscopy (EDS) maps of olivine grains and linear profiles across individual grains from our sample show no evidence of chemical zoning. In addition, linear bands of fluid inclusions were observed within crystals within the dunite (Fig. 3). The solid rock cores allow experimental fluids to pass through natural, pore-network flow paths that are inherent in the rock. Loose particles from coring were removed via brief immersion in an ultrasonic bath, and mass change from fluid-rock reaction was determined by weighing dry cores pre- and post-experiment. Cores were installed into a 1.3 cm i.d. Teflon PFA sheath with a 0.08 cm wall thickness. The Teflon was then wrapped in 0.005 cm stainless steel foil to limit diffusion of gases generated from fluid-rock reaction, and another layer of Teflon PFA held the foil in place.

We conducted two experiments that each lasted slightly more than a month (Table 2). The first experiment was conducted at 150 °C, where artificial seawater was pumped through the dunite core. This fluid was prepared using laboratory-grade reagents (NaCl, $MgCl_2{\cdot}6H_2O$, Na_2SO_4, $CaCl_2{\cdot}2H_2O$, KCl, $NaHCO_3$, $Sr(NO_3)_2$, Li_2CO_3), a Si ($(NH_4)_2SiF_6$) solution, and deionized (DI) water to match seawater composition for these components (Table 3). Because relatively little reaction occurred during the first experiment, the temperature for the second experiment was set higher at 200 °C, and the experimental fluid was enriched in Si to simulate crustal fluids that may have reacted with gabbro bodies in and around detachment fault zones (Boschi et al., 2006, 2008; Seyfried et al., 2015). The slight increase in dissolved Si used for the 200 °C experiment also provides an enhanced driving force for olivine alteration to serpentine/talc, with implications for elucidating the feedback between chemical and physical processes in natural systems. Artificial seawater with enriched Si and Ca was prepared using laboratory-grade reagents (NaCl and $CaCl_2{\cdot}2H_2O$), silica gel, and a B ($(NH_4)_2B_4O_7{\cdot}4H_2O$) solution (Tables 3 and 4). Silica gel was initially dissolved in a high pH NaOH solution before it was mixed with the other artificial seawater components. Both experiments used a flow rate of 0.01 ml/min, an outlet pore-fluid pressure of 150 bar, and a confinement pressure of 200 bar. Given the relatively high flow rate, our experiments are characterized by a state of disequilibrium, with a regime that is more reaction rate-limited than typically found in nature. Attempts were made to remove oxygen from the flow system by repeated evacuation of head space followed by nitrogen pressurization to ≈5 bar. Furthermore, experimental fluid and DI H_2O were exposed to bubbling nitrogen for at least three hours

[1] Calculated using Kurt Hollocher's CIPW Norm Excel program (http://minerva.union.edu/hollochk/c_petrology/norms.htm).

before they were added to the upstream separator and the syringe pumps, respectively.

DI water flowed through the cores before the experiments commenced at experimental temperatures to develop steady-state fluid pressure gradients as well as after the experiments (at 50 °C following Experiment 1 and at room temperature following Experiment 2) to displace residual experimental fluid (artificial seawater) from the cores. Outside of these DI water flow periods, the upstream bypass valve was closed as the valves to the fluid separator were opened to deliver experimental fluid to the core. During the experiments, pressure gradients were continuously recorded and permeability, k, was calculated using Darcy's law (Darcy, 1856):

$$k = -\frac{Q_v \mu L}{A \Delta P}, \quad (1)$$

where Q_v is the volumetric fluid flow rate, μ is the fluid dynamic viscosity, L is the core sample length, A is the cross-sectional area of the core, and ΔP is the pressure drop across the core (over the distance L). Accuracy of the Heise pressure transducers is ±0.125 bar.

Many fluid samples were collected in gas-tight syringes downstream of the reaction cell to identify fluid changes associated with fluid-rock interactions. Collected fluid samples were diluted with nitrogen, and then gas analyses were performed using an Agilent 6890A (G1540A) Gas Chromatograph with uncertainties of ≈5–10% of reported concentrations. The liquid portion of the sample was then filtered with a 0.2 μm filter and split for pH measurements using a ROSS glass electrode at 25 °C (uncertainty of ±0.05 pH units), major cation analysis (acidified with trace metal grade HCl and further diluted with DI H_2O) using ICP-OES (2σ accuracies of 3%), and preservation of diluted, but unacidified samples. Additionally, two unacidified samples from the second experiment were analyzed for major dissolved anions using ion chromatography (IC) to test for the breakdown of Teflon at 200 °C, but neither sample resulted in any measureable fluoride. Expectations of little to no additional information from anion analyses were confirmed by the two analyzed samples. Calcite was identified on the downstream end of the dunite core from Experiment 2 (see below). Because of this, total alkalinity was subsequently measured on the unacidified samples from Experiment 2 by titration with standardized HCl solution to a pH endpoint of 4.5. Speciation and saturation calculations used the LLNL thermo.com.V8.R6+.dat database and Geochemist's Workbench (GWB, version 10.0.3; Bethke and Yeakel, 2015). The DBCreate program was used to modify the database to conform to experimental temperature and pressure conditions (Kong et al., 2013).

Both dunite cores, pre- and post-experiment, were scanned using X-ray computed tomography (XRCT) in the University of Minnesota XRCT Laboratory. An accelerating voltage of 160 kV at a power of 20.0 W was used, and the voxel size was 8 μm × 8 μm × 8 μm.

Connected porosity, ϕ, for both post-experimental cores was determined according to

$$\phi = \frac{S - D}{\rho V}, \quad (2)$$

where S and D are the masses of each saturated and dry core, respectively, ρ is water density, and V is the core volume. Each core was placed in a drying oven at 50 °C for a sufficient time until the mass was constant to determine D. Once dry, the cores were placed in the pressure vessel where gases were evacuated with a vacuum pump and then pressurized with DI H_2O to experimental pore-fluid pressure (150 bar) before returning to atmospheric pressure. S was then determined after the cores were rolled on paper to remove the excess water film around the outer edges of the cores. A digital caliper was used to measure core length and diameter to determine V.

To quantify porosity and surface area of post-experimental dunite core samples and pristine dunite samples over length scales ranging from ≈1 nm to 10 μm, small angle (SANS) and ultra-small angle neutron scattering (USANS) measurements were made following the experiments. (U)SANS has been used to characterize the nm- to μm-scale porosity and surface area of samples from a variety of geological environments (e.g., Anovitz et al., 2009, 2013; Jin et al., 2011; Bazilevskaya et al., 2013; Navarre-Sitchler et al., 2013; Tutolo et al., 2016; Luhmann et al., 2017b). Neutrons efficiently penetrate rock samples, and they elastically scatter when interacting with interfaces consisting of components of different scattering length densities (SLD). In general, the largest SLD difference in a rock occurs between minerals and pores. Mineral–mineral interfaces are often characterized by relatively low SLD differences. Thus, scattering intensities measured over the (U)SANS range are typically dominated by scattering at pore-mineral interfaces, such that the sample can be approximated as a two-phase system of solids and pores (Radlinski, 2006).

150 μm-thick dunite samples were glued (Super Glue) to unfrosted quartz slides, where the thickness limited multiple scattering during (U)SANS measurements (Anovitz et al., 2009). The post-experimental cores from both experiments were sectioned in two along each core's length. Polished sections were prepared (Burnham Petrographics LLC) from these half cores as well as from two pristine dunite samples to compare reacted and pristine samples, and all samples were cut from the same small region of a fist-sized sample.

(U)SANS analyses were conducted at the National Institute of Standards and Technology Center for Neutron Research (NCNR) in Gaithersburg, MD. Analyses record measurements of the scattering intensity, I, which varies with the scattering vector, Q, where $Q = (4\pi/\lambda)\sin(\theta/2)$, λ is the neutron wavelength, and θ is the neutron scattering angle resulting from the neutron passing through the sample. SANS measurements employed the NG7 instrument (Glinka et al., 1998), using pinhole geometry, a two-dimensional detector, and a wavelength spread, $\Delta\lambda/\lambda$, of 0.138. Measurements were made at wavelengths, λ, of 6 Å (with 13.17, 4.0, and 1.0 m distances between the sample and the detector) and 8.4 Å (13.17 m distance with biconcave MgF_2 lenses (Choi et al., 2000)). These instrument settings generate SANS data with a Q range of $\approx 1 \times 10^{-3}$ Å^{-1} to $\approx 3 \times 10^{-1}$ Å^{-1}. USANS measurements employed the

BT5 instrument (Barker et al., 2005), with slit-height geometry, $\lambda = 2.38$ Å, and $\Delta\lambda/\lambda = 0.059$. USANS analysis generated data over a Q range of $\approx 2 \times 10^{-5}$ Å^{-1} to $\approx 2 \times 10^{-3}$ Å^{-1}. SANS and USANS datasets overlap in Q ranges, and together, provide Q data that spans over four orders of magnitude. For both SANS and USANS data collections, neutron-absorbing cadmium masks were adhered to polished section samples (0.15 mm thickness) to ensure measurements were obtained from selected sections of the samples. A cadmium mask with a 3/8 in (0.95 cm) diameter aperture was used with the post-experimental sections, analyzing a volume of ≈11 mm^3. A cadmium mask with a 1/2 in (1.27 cm) diameter aperture was used for the larger pristine sections, analyzing a volume of ≈19 mm^3.

Data processing yielded one-dimensional SANS data via azimuthally averaging (data were axially symmetric) with absolute intensity normalization, following background subtraction of an empty quartz slide measurement and sample transmission correction. Modifications to USANS data included empty-beam and background scattering corrections, absolute intensity normalization, and desmearing using the NCNR Igor Pro macros (Kline, 2006), which was used to reduce and desmear all (U)SANS data. The (U)SANS datasets were then merged and fit using a power law:

$$I(Q) = bQ^{-n} + c, \tag{3}$$

where b is a fitting parameter, the exponent n is the (negative) slope of the scattering curve, and c is the incoherent scattering background. PRINSAS software (Hinde, 2004) was used to subtract the incoherent scattering from the data and to convert the corrected data to a polydisperse, spherical pores (PDSP) and solid distribution. Porosity and specific surface area (SSA) as a function of radius were then calculated from the ensuing pore size distribution. SSA curves were fit with a power law extrapolation to a probe radius of 4 Å, and this value was then divided by dunite density to provide a SSA comparable to BET measurements (Radlinski et al., 2004; Tutolo et al., 2016; Luhmann et al., 2017b), with an uncertainty of ±50% (Radlinski et al., 2004). Additionally, the scattering invariant, Y, can be used to calculate porosity, ϕ, via the following equation (Porod, 1952):

$$Y = \int_0^\infty Q^2 I(Q) dQ = 2\pi^2 (\Delta\rho)^2 \phi(1-\phi), \tag{4}$$

where $\Delta\rho$ is the scattering contrast between the rock and the pore (i.e., the SLD difference). The dunite SLD is 5.153×10^{-6} Å^{-2} (http://www.ncnr.nist.gov/resources/activation/), given the bulk oxide data (Table 1) and dunite density of 3.260 g/cm^3 (Escartín et al., 2001). An air-filled pore has a SLD of zero, and we assume this value for all pores (Anovitz et al., 2013).

The slope in a log I versus log Q plot is the Porod exponent (n in Eq. (3)), representing a fractal when the Porod exponent is constant over a range in Q that spans an order of magnitude at minimum (Radlinski et al., 1996). A Porod exponent between 2 and 3 indicates a mass fractal, where the mass fractal dimension, D_m, is given by the exponent (i.e., $D_m = n$). A mass fractal describes an object of length, l, where the mass scales as l^{Dm}. When the Porod exponent is between 3 and 4, a surface fractal exists, with a surface fractal dimension given by $D_s = 6 - n$. The surface area of a surface fractal object varies as l^{Ds}. This change in the Porod exponent has been discussed by Mildner and Hall (1986) in terms of fractal geometry applied to pores within geologic material. To determine the Porod exponent, we employ a standardized major axis regression (Warton et al., 2006, 2012) in R (R Core Team, 2016), where we partition data used in fits by minimizing the mean squared error of sections that span at least one order of magnitude in Q.

Thin sections were made from both post-experimental cores and the pristine sample for thin section microscopy analysis. A JEOL JSM-6500F scanning electron microscope (SEM) was used to image mineral surface and thin section changes, using an accelerating voltage of 15–20 kV, a probe current of 5–20 nA, and a working distance of 10 mm. An Oxford X-Max 80 EDS was used to identify experimental alteration by comparing chemical analyses of the thin sections created from the Experiment 2 core and the pristine sample. EDS analyses employed one million counts full spectrum, using Oxford Instruments Aztec software.

Vibrating sample magnetometer (VSM) measurements were performed on representative portions of both post-experimental cores (4.196 g and 3.384 g of the Experiment 1 and Experiment 2 cores, respectively) to determine the presence and amount of magnetite from fluid-rock reaction. VSM analyses were also performed on two pristine samples (≈ 4.5–5 g) to facilitate comparison to reacted cores. The VSM measures the induced magnetization of the sample, and wt% of magnetite, m_{mag}, is estimated by

$$m_{mag} = \frac{M_{s,sam}}{M_{s,mag}} \times 100, \tag{5}$$

where $M_{s,sam}$ and $M_{s,mag}$ are the saturation magnetizations (i.e., the maximum induced magnetic moment in a magnetic field) of the sample and magnetite, respectively. Based on previous magnetic analyses of experimental serpentinization products (Malvoisin et al., 2012a), we assume pure magnetite in the magnetite calculation. The hysteresis data collected with the VSM is sensitive to all sizes of magnetic minerals. The sensitivity of the instrument is 5×10^{-9} A m^2, which means masses of magnetite as small as 54 ng and masses of hematite as small as 12500 ng can be detected. VSM measurements were conducted using a Princeton Measurements Corporation Vibrating Sample Magnetometer at the Institute for Rock Magnetism (IRM) at the University of Minnesota. The saturating field was 1 T, and measurements were made at room temperature. Data were processed using methods described by Jackson and Solheid (2010).

X-ray absorption near edge structure (XANES) spectra were acquired on one of the pristine and the post-Experiment 2 150 μm-thick dunite sections at Diamond Light Source on the I18 beamline using a 10 μm X-ray beam over the energy range 7000–7300 eV, with 0.1 eV spacing and count times of five s in the pre-edge region (7100–7118 eV) and step sizes of 1–10 eV and count times

of one s in the surrounding regions. Double-crystal silicon monochromator in the Si(333) reflection configuration was used to increase the beamline energy resolution compared to the standard Si(111) configuration. Energy calibration was confirmed by measuring Fe metal foil, and all data collection was performed in fluorescence mode with the pristine and post-Experiment 2 sections positioned at a 45° angle from the incident beam. A 115 μm-thick Al foil was placed in the beam path to reduce the incident X-ray flux, and a 200 μm-thick diamond filter was positioned before the monochromator to reduce the thermal load and attenuate the incident X-ray flux further. A lack of measurable photo-oxidation of Fe during data collection was confirmed by monitoring the measured absorbance at the Fe(II) and Fe(III) pre-edge peak energy positions of a completely serpentinized peridotite as a function of time over a period of several minutes. Prior studies (Wilke et al., 2001; Marcaillou et al., 2011; Andreani et al., 2013b; Miller et al., 2017) have shown that the centroid of the pre-edge region can be used as a quantitative measure of the oxidation state of Fe in serpentinites, provided that Fe(II)- and Fe(III)-bearing model compounds are additionally analyzed for calibration purposes. Following the guidelines put forth by these authors, we processed our spectra by first subtracting the average of the background absorbance acquired between 7000 and 7050 eV and then normalizing the intensity to the average absorbance measured between 7250 and 7300 eV. Pre-edge features were extracted by subtracting a spline function fit to the normalized absorbance measured above and below the features, whose positions changed depending on the bulk oxidation state of the analyzed sample. These features were then fit using a set of Gaussian peaks and compared to fits of spectra acquired on Fe(II)-bearing San Carlos olivine (NMNH 111312-44) and Fe(III)-bearing andradite garnet (NMNH 166396) provided by the Smithsonian Institution National Museum of Natural History.

Finally, Fourier transform-infrared (FT-IR) spectroscopic analysis was performed on one of the pristine and the post-Experiment 2 150 μm-thick dunite sections to identify experimental alteration, using a PerkinElmer Spotlight 200i FT-IR microscope in reflectance mode, scanning over wave numbers from 600 to 4000 cm^{-1} for one minute per spot. Due to the limited amount of alteration phases in both the pristine and post-Experiment 2 dunite samples, all spectra represent combinations of primary igneous and alteration mineralogy. Grain boundaries and cracks within crystals were analyzed using narrow (10 μm) aperture widths on polished section samples with heights from up to ≈100 μm in order to fill as much of the analyzed area with the alteration phase of interest. Background-subtracted spectra were compared to published spectra (Chukanov, 2014) to identify minerals.

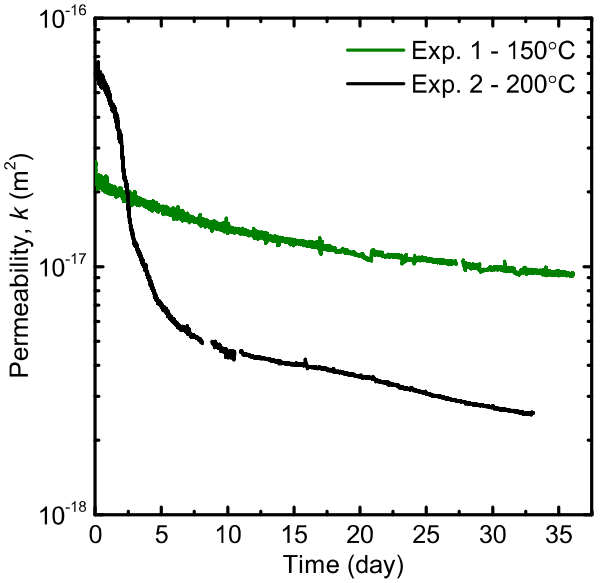

Fig. 4. Permeability decreased for both experiments as a function of time, although there was a significant difference in the decrease between the two experiments.

3. RESULTS

Permeability decreased for both experiments with reaction progress (Fig. 4 and Table 2). During Experiment 1 at 150 °C, permeability decreased by a factor of 2.4 over the 36 day experiment. During Experiment 2 at 200 °C, permeability decreased by a factor of 25. Much of the permeability decrease occurred over the first four days of Experiment 2, but there was still a gradual and steady decrease in permeability over the final 29 days of the experiment. Error bars in permeability measurements that arose from uncertainty with the pressure transducers generally ranged from ±30% with the relatively low pressure differences between the upstream and downstream ends of the core at the beginning of Experiment 2 to ±1% at the end of this experiment with the increasing pressure gradient. Permeability data are provided as Supplementary Data.

There was a visible change in the color of the post-experimental cores, although the change was more obvious for the core from the second experiment at 200 °C (Fig. 5). During Experiment 1 at 150 °C, the core appeared slightly bleached with respect to the initial light green starting mate-

Table 2
Experiment and core details.

Experiment	Flow rate (ml/min)	Duration (day)	Core diameter (cm)	Core length (cm)	Pre-experiment mass (g)	Post-experiment mass (g)	Mass balance change (g)	Post-experiment connected porosity (%)	Initial permeability (m^2)	Final permeability (m^2)
1	0.01	36.09	1.26	2.68	10.024	10.032	+0.01	2.7	2.2×10^{-17}	9.3×10^{-18}
2	0.01	32.99	1.26	2.62	9.949	9.972	+0.05	3.0	6.4×10^{-17}	2.58×10^{-18}

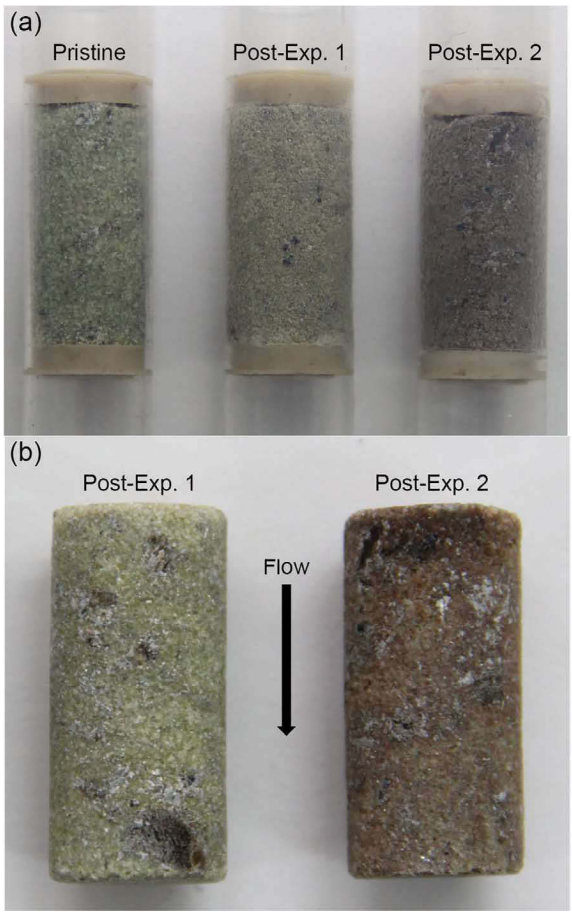

Fig. 5. The post-experimental cores shown (a) with and (b) without the Teflon sheath and the PEEK retainer rings. Whereas the post-Experiment 1 core was slightly bleached with respect to the pristine dunite (a), the post-Experiment 2 core became brown from experimental alteration. Cores are 1.26 cm in diameter (Table 2).

rial. In contrast, at 200 °C, reaction between the dunite and evolved seawater modified the green color to a brown color along the entire length of the core (giving it the characteristic "dun" color for which dunite is named), with an enhanced darker reddish brown color at the upstream end.

There was relatively little change to the seawater solution as it passed through the core during the first experiment at 150 °C, but considerably greater change in fluid chemistry was recognized during the second experiment at 200 °C (Fig. 6 and Table 3). Specifically, Mg was continuously released over the duration of this experiment, while outlet Si yielded concentrations that were either below or above the initial fluid composition (Fig. 6). During Experiment 2, the initial experimental fluid had essentially no Mg. The first collected outlet sample had a concentration of 0.76 mmol/kg, but quickly decreased to concentrations of 0.2 mmol/kg or less. Our experimental source fluid had a Si concentration of 1.63 mmol/kg. Si decreased to half of its initial value during the first four days of Experiment 2. After this initial period, Si then increased to a concentration of 2.05 mmol/kg, which was higher than the starting fluid, before decreasing to a concentration of 1.0 mmol/kg throughout the remainder of the experiment. The starting fluid had a pH (200 °C) of 7.91 (Fig. 6 and Table 4), where pH (200 °C) is pH measured at room temperature and then converted to pH at 200 °C using speciation constraints and Geochemist's Workbench (Bethke and Yeakel, 2015) with mineral reactions suppressed. The first sample collected at the outlet had a pH (200 °C) of 5.97, but most samples produced a pH (200 °C) of 7.0–7.3 downstream of the core. At 200 °C, neutral pH is 5.66 (Bandura and Lvov, 2006), so all samples were slightly basic. Previous research has noted incorporation of B into secondary phases during serpentinization at relatively high pH (Seyfried and Dibble, 1980; Boschi et al., 2008; Foustoukos et al., 2008), and minor B uptake may have occurred at the pH of this experiment. There was a decrease in Na (concentration was ≈90% of the starting fluid) with the two samples collected at 4.65 and 6.64 days. However, this decrease was due to dilution (which was also observed with the Cl concentration at 6.64 days), as the decrease corresponds to a four- to five-day period (indicated by a gradual water volume decrease in Pump C) where DI water from the confinement fluid momentarily diluted the pore fluid by ≈10%.

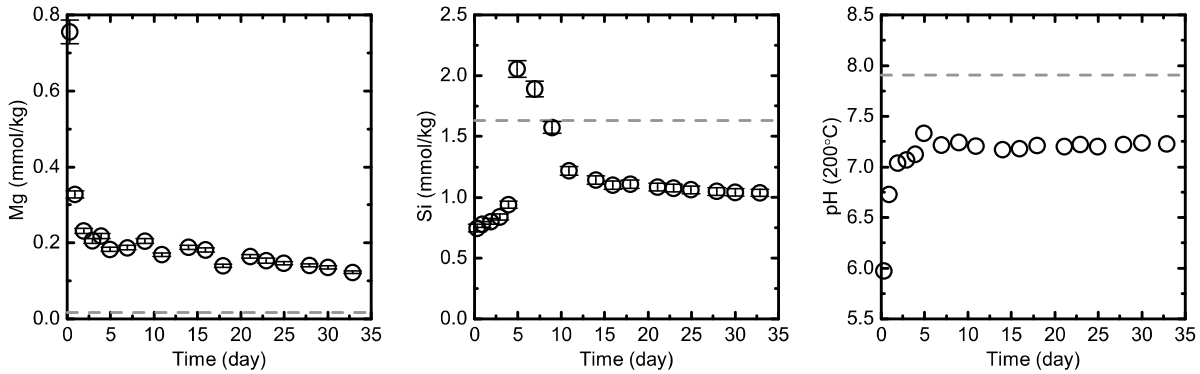

Fig. 6. Mg, Si, and pH (200 °C) as a function of time during Experiment 2. Mg was continuously released and outlet Si concentrations were either below or above the initial solution composition during this experiment. The dashed lines represent the concentrations or pH (200 °C) of the initial experimental solution, and Mg and Si error bars indicate 2σ error.

Table 3
Outlet fluid chemistry.

Time day	B μmol/kg	Ba μmol/kg	Ca mmol/kg	Fe μmol/kg	K mmol/kg	Li μmol/kg	Mg mmol/kg	Mn μmol/kg	Na mmol/kg	Si μmol/kg	Sr μmol/kg	Zn μmol/kg
Experiment 1: 150 °C												
Starting fluid	n.a.	1.40	9.9	<DL	10.4	24.3	53	<DL	460	80	93	1[a]
0.02	n.a.	1.54	5.1	<DL	6.1	16.6	27.9	47	300	80	49	48
0.60	n.a.	0.6	9.6	<DL	10.4	25	51	11.9	460	<DL	91	41
1.60	n.a.	1.0	10.4	60[a]	10.5	25.9	52	9[a]	470	900[a]	93	22
2.63	n.a.	0.41	9.9	7[a]	10.5	25.7	53	3.3	470	<DL	94	18.8
3.61	n.a.	0.39	9.9	<DL	10.5	25.0	52	2.4	460	70	94	70
7.60	n.a.	0.38	9.9	<DL	10.4	25.2	53	1.3	460	40	94	71
11.62	n.a.	0.36	9.9	<DL	10.4	24.4	53	1.0	460	36	94	10
18.63	n.a.	0.36	9.9	<DL	10.5	24.6	53	0.8	460	20[a]	94	4
26.60	n.a.	0.37	10.0	<DL	10.6	24.3	53	0.6[b]	460	30[a]	94	3[b]
33.61	n.a.	0.37	9.9	<DL	10.6	26.8	53	0.5[a]	460	24[b]	94	3
35.60	n.a.	0.37	9.8	<DL	10.6	23.9	53	0.6	460	32	93	3.4
Experiment 2: 200 °C					μmol/kg					mmol/kg		
Starting fluid	410	0.32	33	8	21	2.4	0.017	<DL	450	1.63	8.4	<DL
0.06	250	0.44	20.2	6	59	2.5	0.76	1.2	330	0.75	5.6	2[a]
0.65	370	0.32	30.1	<DL	51	2.9	0.33	0.4[b]	440	0.78	8.1	0.9[a]
1.65	380	0.37	31.0	<DL	37	2.8	0.231	0.3[b]	440	0.80	8.3	<DL
2.65	390	0.37	31.2	<DL	30	4.7	0.205	0.2[a]	440	0.84	8.3	<DL
3.65	410	0.41	32	11	2[a]	2[a]	0.218	0.4[b]	450	0.94	8.5	<DL
4.65	340	0.37	29.7	4[b]	12[a]	3[b]	0.183	0.5[b]	410	2.05	8.9	<DL
6.64	340	0.36	29.4	3[b]	9[a]	2[a]	0.187	0.7	400	1.89	8.6	<DL
8.65	390	0.33	31.6	7	4[b]	2[a]	0.205	0.4[a]	440	1.58	8.5	1[a]
10.63	360	0.33	31.6	4[b]	52	2.6[b]	0.169	0.5[b]	450	1.22	9.3	1.4[a]
13.81	410	0.32	32	7[b]	1[a]	2[a]	0.188	0.4[a]	450	1.14	8.4	<DL
15.78	410	0.32	32	7	3[a]	<DL	0.182	<DL	460	1.10	8.5	2[a]
17.78	380	0.34	32	3[b]	6[a]	2.4[b]	0.140	0.5	450	1.11	9.1	2[a]
20.90	420	0.30	32	7[a]	0.8[a]	2[a]	0.164	<DL	470	1.08	8.3	1.9[a]
22.73	430	0.26	32	10	<DL	1[a]	0.153	<DL	460	1.08	8.5	3[b]
24.73	400	0.26	32	7	2[a]	<DL	0.146	<DL	450	1.06	8.5	2[b]
27.71	390	0.30	32	8[b]	5[b]	<DL	0.141	<DL	450	1.05	8.6	1.9[b]
29.84	370	0.3[b]	32	8	0.8[a]	<DL	0.135	<DL	450	1.04	8.5	1.6[a]
32.70	380	0.26	32	7[a]	1.2[a]	1[a]	0.122	<DL	440	1.04	8.4	2[a]

n.a. = not analyzed, DL = detection limit.
[a] Analyzed value is not larger than 2 × the 2σ error.
[b] Analyzed value is not larger than 3 × the 2σ error.

Table 4
Outlet pH, gas, alkalinity, and Cl chemistry.

Time day	pH 25 °C		H_2 μmol/kg	CH_4 μmol/kg	CO μmol/kg	CO_2 μmol/kg	Alk. mmol/kg	Cl mmol/kg
Experiment 1: 150 °C								
Starting fluid	7.8		n.a.	n.a.	n.a.	n.a.	n.a.	n.a.
0.02	n.a.		<DL	<DL	1.01	531	n.a.	n.a.
0.60	6.94		<DL	<DL	<DL	287	n.a.	n.a.
1.60	6.94		17	<DL	<DL	131	n.a.	n.a.
2.63	6.94		21	0.15	<DL	98	n.a.	n.a.
3.61	7.16		35	0.49	<DL	75	n.a.	n.a.
5.65	7.12		35	0.84	0.05	85	n.a.	n.a.
7.60	7.19		30	0.95	0.06	72	n.a.	n.a.
9.60	7.14		29	0.95	0.04	50	n.a.	n.a.
11.62	7.28		34	1.22	<DL	83	n.a.	n.a.
13.59	7.21		30	1.23	<DL	53	n.a.	n.a.
15.63	7.26		28	1.29	<DL	58	n.a.	n.a.
18.63	7.33		28	1.10	<DL	79	n.a.	n.a.
21.63	7.31		29	1.52	<DL	66	n.a.	n.a.
23.61	7.29		33	2.09	0.29	71	n.a.	n.a.
26.60	7.30		28	12.9	11.7	96	n.a.	n.a.
28.59	7.30		30	3.7	1.88	80	n.a.	n.a.
30.61	7.26		26	1.59	<DL	72	n.a.	n.a.
32.62	7.37		19	1.33	<DL	94	n.a.	n.a.
33.61	7.25		36	20.7	19	111	n.a.	n.a.
34.60	7.25		26	1.71	<DL	84	n.a.	n.a.
35.60	7.25		19	1.42	<DL	91	n.a.	n.a.
Experiment 2: 200 °C		pH (200 °C)						
Starting fluid	10.5	7.91	n.a.	n.a.	n.a.	n.a.	3.66	540
0.06	6.38	5.97	262	137	<DL	338	1.55	n.a.
0.65	6.88	6.73	451	247	<DL	18	0.92	530
1.65	8.11	7.04	534	245	<DL	10	0.89	n.a.
2.65	8.18	7.07	579	235	<DL	8	0.88	n.a.
3.65	8.28	7.13	601	223	<DL	6	0.97	n.a.
4.65	8.35	7.33	619	249	<DL	9	1.14	n.a.
6.64	8.13	7.21	611	271	<DL	6	1.09	500
8.65	8.30	7.24	551	258	<DL	8	1.05	n.a.
10.63	8.36	7.21	500	245	<DL	13	0.98	n.a.
13.81	8.29	7.17	484	260	<DL	13	0.98	n.a.
15.78	8.30	7.18	425	257	<DL	16	1.07	n.a.
17.78	8.44	7.21	457	272	<DL	16	0.89	n.a.
20.90	8.46	7.20	496	319	<DL	16	0.71	n.a.
22.73	8.49	7.22	418	298	<DL	30	0.87	n.a.
24.73	8.46	7.20	390	299	<DL	20	0.79	n.a.
27.71	8.51	7.22	357	296	<DL	14	0.91	n.a.
29.84	8.57	7.23	379	329	<DL	19	0.89	n.a.
32.70	8.54	7.23	302	287	<DL	17	0.93	n.a.

n.a. = not analyzed, DL = detection limit.

The core mass of both cores increased slightly during the experiments, with the Experiment 1 core increasing by 0.008 g and the Experiment 2 core increasing by 0.023 g (Table 2). Mass balance calculations are generally consistent with this minor mass increase and predict an increase of 0.01 g for Experiment 1 and 0.06 g for Experiment 2 (or 0.01 g and 0.05 g, respectively, when correcting samples with low Na concentrations for dilution effects). The mass balance calculations employed all major chemistry in Table 3 except for dissolved Na, which was excluded from the calculation because the error of the Na concentration associated with the seawater solution would exceed any change in dissolved Na from experimental alteration.

Samples from Experiment 2 were generally supersaturated with respect to tremolite, talc, chrysotile,[2] and calcite (Fig. 7). Talc was always more supersaturated than chrysotile, but fluids were generally characterized by a log $\Omega > 4$ for talc and chrysotile, where

[2] Chrysotile is employed here instead of lizardite, but the two polymorphs have similar thermodynamic data (e.g., Frost and Beard, 2007).

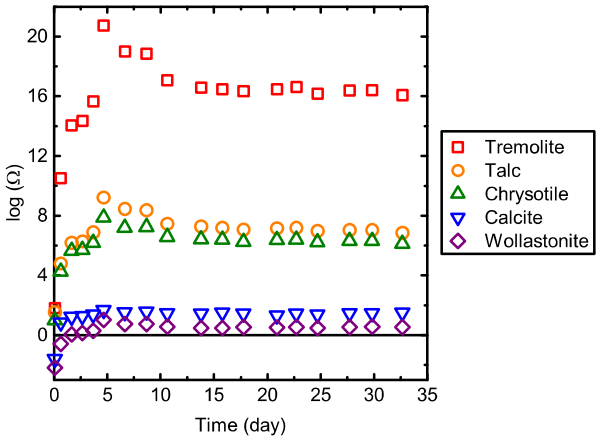

Fig. 7. Saturation index, Ω, as a function of fluid volume for Experiment 2. Most samples were supersaturated with respect to tremolite, talc, chrysotile, and calcite.

$$\Omega = \frac{IAP}{K} \tag{6}$$

is the saturation index, IAP is the ion activity product, and K is the equilibrium constant. All of these samples were generally near saturation with respect to wollastonite.

Both experiments produced H_2 and CH_4 (Table 4). Fig. 8 depicts time series changes of these dissolved gases with reaction progress for Experiment 2. During Experiment 1 at 150 °C, H_2 and CH_4 were more than one and two orders of magnitude lower, respectively, than Experiment 2 at 200 °C. During Experiment 2, H_2 increased to a peak concentration of 619 μmol/kg before gradually decreasing to a concentration of 302 μmol/kg at the end of the experiment. CH_4 generally increased throughout this experiment and ultimately reached concentrations of ≈300 μmol/kg. No attempt was made to analyze for dissolved gases in the confinement fluid in the pressure vessel; however, both H_2 and CH_4 were detected from samples collected from Pump C post-experiment, suggesting that concentrations of H_2 and CH_4 in outlet fluids are minima due to diffusion of gases through the Teflon sleeve and into the confinement fluid. In addition, we conducted a blank experiment to test for H_2 production potentially arising from oxidation of stainless steel and copper components within the reaction cell. During this test, an attempt was made to remove air in the headspace of the reaction cell, and it was pressurized to 200 bar and heated to 200 °C. Three fluid samples were collected in the following days, and H_2 was always an order of magnitude lower than the values measured during Experiment 2.

Secondary electron SEM images were collected from pristine olivine grains that did not react with experimental fluid as well as from the post-experimental cores (Fig. 9). Pristine olivine grains are relatively clean and are surrounded by a secondary mineral layer that is in direct contact with surrounding grains in all directions (Fig.9a), illustrating the low porosity of the sample. Most of the pores that do exist likely occur where three or more grains join (Wark et al., 2003). Both ends from the 200 °C experiment included clear evidence of secondary mineralization. At the upstream end, olivine grains were covered in a secondary phase with a honeycomb-like texture (Fig. 9b and c). Calcite formed on the downstream portion of the core during this same experiment, illustrated by crystal rhombs on mineral surfaces (Fig. 9d). Unlike the upstream portion, the downstream end did not contain the honeycomb-textured alteration. There may have been secondary mineralization during Experiment 1 at 150 °C, but it was much less than occurred during Experiment 2.

Secondary electron SEM images were also collected from the thin sections created from the post-Experiment 2 core and the pristine dunite (Fig. 10). Images from the Experiment 2 section showed parallel, linear grooved features with a discontinuous texture at the upstream end and near the core edges that was more characteristic of dissolution features rather than cracks (Fig. 10c and d). While the linear dissolution features appear discontinuous in 2D, they are likely continuous in 3D as the dissolution features move into and out of the polished 2D surface. The pristine dunite did not show this texture (Fig. 10a and b), which indicates that the features on the Experiment 2 section were

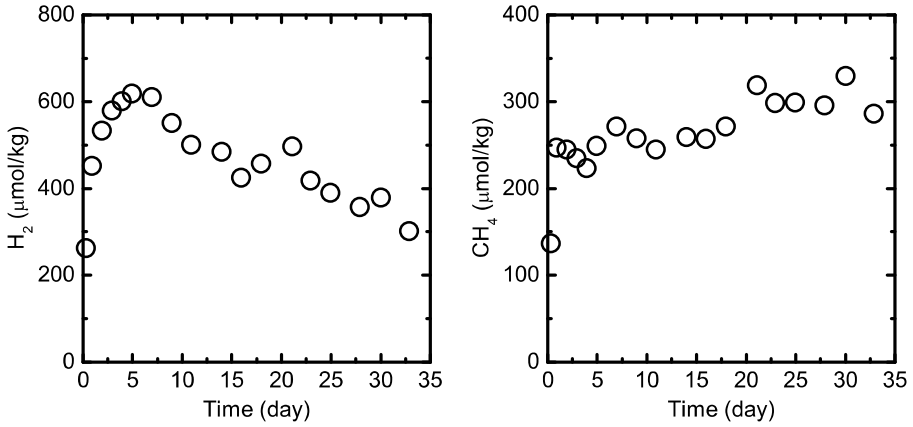

Fig. 8. H_2 and CH_4 as a function of time during Experiment 2. H_2 and CH_4 were more than one and two orders of magnitude higher, respectively, during Experiment 2 at 200 °C than they were during Experiment 1 at 150 °C.

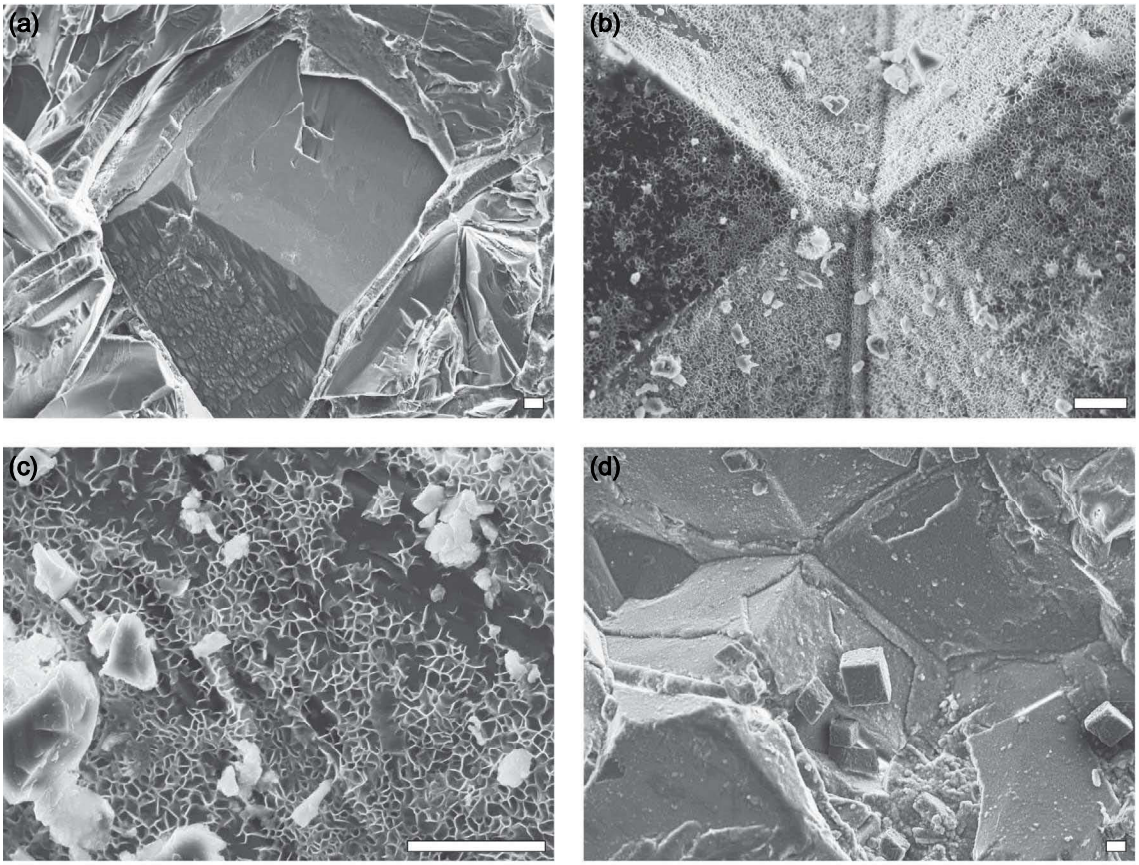

Fig. 9. Secondary electron SEM micrographs of (a) pristine and (b-d) post-experimental dunite from Experiment 2. (a) Pristine grain portrays a relatively clean olivine surface with a layer of secondary mineralization that is in contact with surrounding grains, resulting in low porosity. (b and c) Crystals at the upstream end of the post-experimental core from Experiment 2 were covered in a honeycomb-like texture. (d) Calcite rhombs were abundant on mineral surfaces on the downstream end of the post-experimental core from Experiment 2. Each micrograph includes a 10 μm scale bar.

not an artifact of preparation of the thin section. Still, cracks existed within individual pristine dunite crystals (Fig. 10b).

EDS spot analyses of the pristine dunite and post-Experiment 2 thin sections generally indicate that primary and secondary phases contain Fe, but are dominated by O, Mg, and Si (Table 5). Secondary phases from both thin sections generally contain more O and less Mg than primary olivine crystals, although alteration minerals show both enrichments and depletions of Si and Fe when compared to primary olivine. Several of the alteration phase analyses yielded a (Mg + Fe)/Si of ≈1.5, indicative of the mineral serpentine. While Cl was never detected in any pre-existing alteration phases of the pristine dunite thin section, many EDS spot analyses on the secondary phases of the post-experimental section from Experiment 2 indicated slight uptake of Cl in the serpentine (Table 5), indicating serpentine formation during the experiment. Previous research has noted Cl uptake during serpentine precipitation (Mével, 2003; Sharp and Barnes, 2004; Seyfried et al., 2015), and this Cl signature did not result from residual artificial seawater left in the core because there was no detection of Na. One EDS spot analysis was collected on a partially dissolved olivine crystal from the Experiment 2 section (on one of the linear dissolution features, as shown in Fig. 10c and d), yielding an O and Mg composition intermediate between the pristine olivine crystals and most of the secondary crystals. In addition, this analysis showed a more significant Fe depletion in the olivine than either the Mg or Si, suggesting that Fe was preferentially removed from the olivine crystals during their dissolution. All collected EDS analyses with pictures are provided as Supplementary Data.

At the end of Experiment 2, a white precipitate was identified in the piston assembly upstream of the experimental core (Fig. 11). 0.0033 g of this precipitate was recovered. While there was additional precipitate that was not recovered, it is unlikely that there was more than two times of the recovered mass in total. An ICP-OES analysis generally indicated that this phase was rich in Ca and Si (Table 6). While the total wt% was much greater than 100% (due to the uncertainty of dissolving a small mass that was a portion of the minor recovered precipitate), this secondary phase is likely wollastonite, especially given the mineral tex-

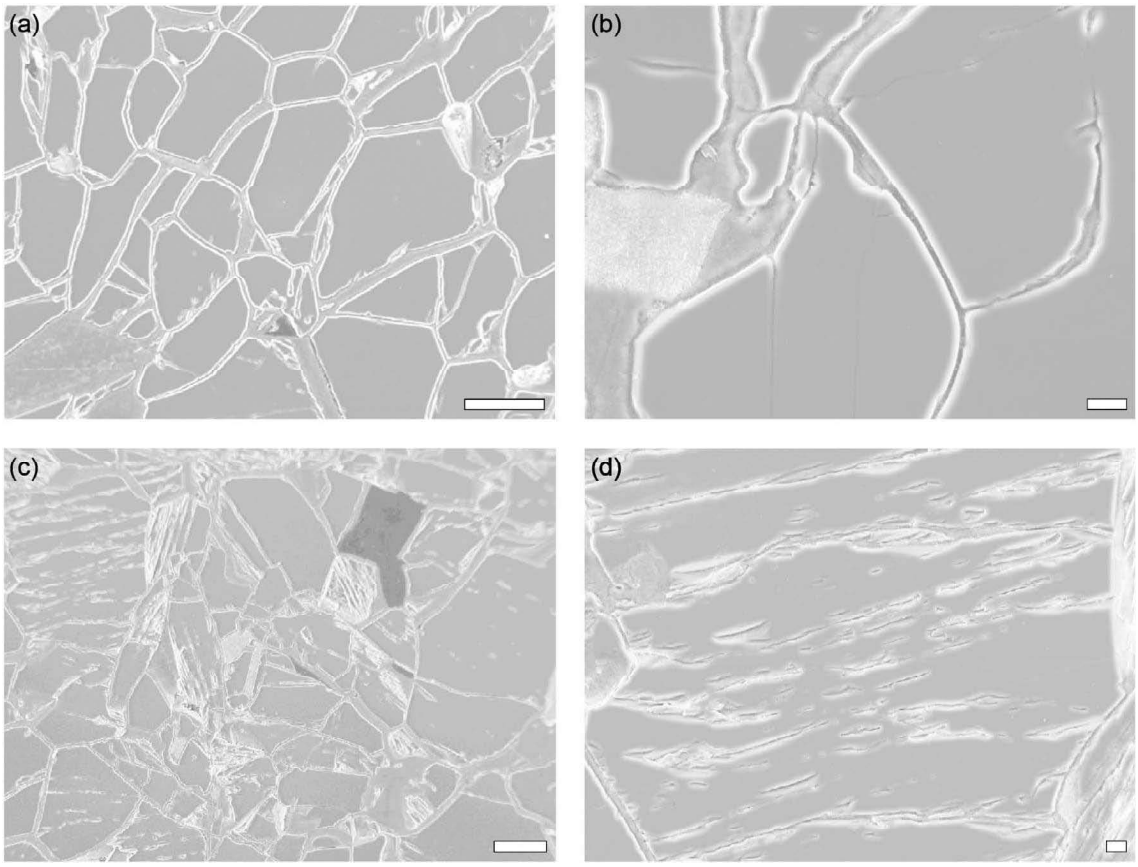

Fig. 10. Secondary electron SEM micrographs of thin sections of (a and b) pristine and (c and d) post-experimental dunite from Experiment 2. (a) Crystals in the pristine thin section contain smooth surfaces, (b) but occasional cracks are visible within individual crystals. (c) Linear features were observed across crystals in the post-experimental dunite. (d) The linear features are discontinuous grooves, with a texture that suggests dissolution along focused bands. The white scale bar is 100 μm in (a) and (c) and 10 μm in (b) and (d).

ture (Fig. 11). Furthermore, five qualitative EDS spot analyses on unpolished surfaces of this precipitate indicated that Ca, Si, and O make up 97.7%–100% of these crystals.

VSM analyses indicated a slight enrichment in magnetite for the post-experimental core from Experiment 2 with respect to the pristine samples (Table 7). The wt% of magnetite in the post-experimental core from Experiment 1 fell within the range of the amount of magnetite in the pristine samples. Multiplying the magnetite wt% (Table 7) by the post-experimental core mass (Table 2) gives 0.55 and 1.22 mg of magnetite in the post-experimental cores from Experiment 1 and Experiment 2, respectively. When hematite is present, it appears in hysteresis loops as high coercivity grains that produce an opening in the loop up to fields higher than 300 mT, as well as a notable slope at fields higher than 300 mT. However, none of the measured loops showed evidence of hematite.

Fe K-edge XANES spectroscopy indicated Fe oxidation during Experiment 2 (Fig. 12), given by four spectra of the pristine dunite and three spectra of the post-Experiment 2 dunite sample. In addition, three and two spectra were attained for the San Carlos olivine and andradite garnet, respectively, to compare the dunite spectra to Fe(II) (San Carlos olivine) and Fe(III) (andradite garnet) mineral phases. While the 10 μm beam size necessarily incorporated primary mineral phases in the spectra, there was a significant shift in the centroid of the pristine dunite spectra, due to the presence of significant ferrous Fe, to the centroid of the post-Experiment 2 spectra, indicating an increase in ferric Fe (Fe(III)) in the alteration phases of the post-experimental sample (Fig. 12 and Table 8).

Ten FT-IR spectra were obtained for both the pristine and post-experiment dunite from Experiment 2. Four spectra (two from each sample) are shown in Fig. 13, illustrating change from experimental alteration during Experiment 2. The other eight spectra from both samples looked similar to the pristine spectra shown in the figure. In the pristine sample spectra, the lattice vibration region surrounding 1000 cm^{-1} is dominated by primary igneous olivine (885 and 985 cm^{-1}) and pyroxene (944 cm^{-1}), while the ≈3700 cm^{-1} band and the presence of Mg-Si bonds in the lattice vibration region are consistent with a serpentine mineral such as antigorite or potentially lizardite. Experiment 2 spectra, on the other hand, illustrate that the sample gained a considerable amount of physically adsorbed water during the experiment, as evidenced by introduction of the broad band at around 3250 cm^{-1} (Pokrovsky and Schott, 2000), indicating additional serpentine formation. Moreover, the

Table 5
EDS spot analyses of primary and secondary crystals of pristine dunite and post-Experiment 2 dunite. All values are listed as at%.

			O	Mg	Si	Fe	Al	Ca	Cl	Cr	Mn	Ni	Zn
Pristine dunite	*Primary crystals*	Olivine	54.7	27.6	15.2	2.5						0.1[a]	
		Olivine	54.5	27.7	15.2	2.5					0.1[a]	0.1[a]	
		Olivine	54.5	27.6	15.3	2.5						0.1[a]	
		Olivine	54.8	27.5	15.1	2.5						0.1[a]	
		Pyroxene	57.6	19.2	21	1.8	0.2	0.1[a]			0.1[a]		
		Pyroxene	58.5	19	20.4	1.7	0.4			0.1[a]			
		Pyroxene[b]	59.9	12.9	20.7	0.6	0.6	5		0.2			
		Chromite	54.7	4.8	0.4	14.8	3.8			21.3			0.1[a]
	Secondary crystals		61.9	21.2	14.9	2							
			61.3	21.3	15.2	2						0.1[a]	
			62.7	20.9	14.8	1.5							
			59.2	19.1	19.9	1.6					0.1[a]		
			59.5	19	19.9	1.6					0.1[a]		
			60	19.4	12.6	1	6			1		0.1[a]	
			62.1	18.1	11.2	1	6.6			0.8		0.1[a]	
			62.2	18.1	11.2	1	6.7			0.7		0.1[a]	
		[c]	56.3	14.4	17.4	5.9	1.1	2.7	0.1[a]		0.2[a]	0.2[a]	0.2[a]
			58.4	19.3	20.5	1.7					0.1[a]		
			60.4	16.2	23	0.3						0.1[a]	
			58.7	16.9	24	0.3						0.1[a]	
Post-Exp. 2	*Primary crystals*	Olivine	55	27.4	15	2.4						0.1[a]	
		Olivine	54.9	27.5	15	2.5						0.1[a]	
		Olivine	55	27.4	15	2.5						0.1[a]	
		Olivine	54.5	27.6	15.3	2.5						0.1[a]	
		Olivine	55.1	27.4	15	2.4						0.1[a]	
		Olivine	54.7	27.5	15.2	2.5						0.1[a]	
		Partially dissolved olivine	58.7	25.7	13.6	1.8						0.1[a]	
		Pyroxene	59.7	16.5	21.4	2.1				0.2	0.1[a]		
		Pyroxene	59.5	13.2	21.2	0.5	0.3	5.1		0.2			
		Chromite	55	4.3	0.7	17.4	1.4			21			0.1[a]
		Phyllosilicate	61.8	18.7	12.1	1.2	5.6			0.5			
	Secondary crystals		61	21.7	15.2	1.8			0.1			0.1[a]	
			61.9	21.4	14.9	1.7			0.1[a]				
			61.2	21.4	15.2	2			0.1			0.1[a]	
			61.7	21.3	14.9	1.9			0.1			0.1[a]	
			61.8	21	15.3	1.8			0.1			0.1[a]	
			62	21.3	14.5	1.9			0.1			0.1[a]	
			61	21.8	15.2	1.9			0.1				
			61.9	21.5	14.9	1.6			0.1				
			62.7	21.3	14.3	1.6			0.1				
			62	21.3	14.8	1.9			0.1[a]				
			61	21	15.6	2			0.3			0.1[a]	
			59.7	21.5	16.2	2.3			0.1			0.1[a]	
			60.2	21.3	15.9	2.4			0.1			0.1[a]	
			59.3	22.1	16	2.3		0.1[a]	0.1			0.1[a]	
			46.2	26.2	21.3	4.8	0.2[a]	0.1[a]	0.4		0.1[a]	0.7	
			62.6	18	11.4	0.9	6.4			0.6		0.1[a]	
			59.7	19	13	1	6.3	0.1[a]		0.8		0.1[a]	
			61.6	18.3	11.5	1.1	6.7			0.7			
			29.1	29.2	29.8	8.7		0.1[a]	2.4		0.1[a]	0.5	
			58	17	24.4	0.4			0.1[a]			0.1[a]	
			59.5	16.8	23.3	0.3						0.1[a]	
			58.1	17	24.3	0.4						0.1[a]	
			60.3	16.6	22.7	0.3						0.1[a]	
			60.4	16.5	22.7	0.3						0.1[a]	

[a] Analyzed wt% value is not larger than 10× the σ error.
[b] Spot analysis also yielded the following: Sc – 0.1[a].
[c] Spot analysis also yielded the following: K – 0.7; Na – 0.5; S – 0.1[a]; Ti – 0.2[a].

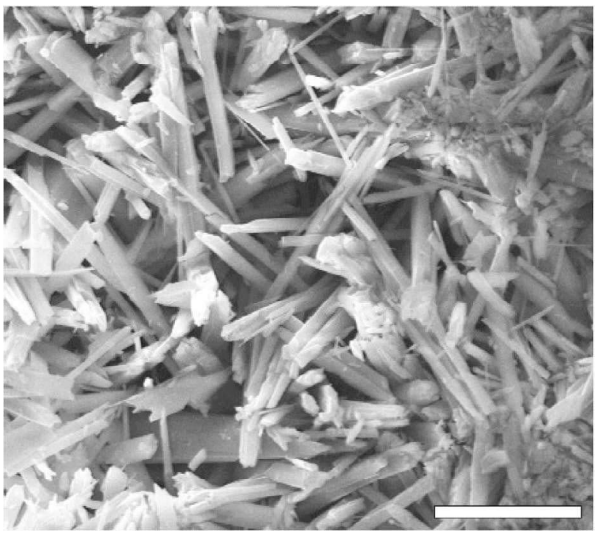

Fig. 11. SEM micrograph of a secondary mineral recovered in the upstream piston assembly. Morphology and composition (ICP-OES oxide and EDS spot analyses indicate a composition rich in Ca and Si) suggest wollastonite. The white scale bar is 10 μm.

Table 6
Chemical composition of precipitate in the upstream piston assembly following Experiment 2.

Oxide	wt%
Al_2O_3	0.19[a]
CaO	67
Cr_2O_3	0.19
FeO	0.22
K_2O	0.018[a]
MnO	0.0036
NiO	0.039
SiO_2	73
TiO_2	0.31
ZnO	0.077
Total	141

[a] Analyzed value is not larger than 3× the 2σ error.

Table 7
Vibrating sample magnetometer (VSM) analyses.

Sample	Magnetite (wt%)
Pristine 1	6.34×10^{-3}
Pristine 2	4.66×10^{-3}
Post-Exp. 1	5.50×10^{-3}
Post-Exp. 2	1.22×10^{-2}

development of a sharp peak at 1017 cm^{-1} in the Experiment 2 sample suggests the presence of talc (1017 cm^{-1}) or saponite (1020 cm^{-1}). The Experiment 2 sample spectra also exhibit the introduction of a band at 1690 cm^{-1}, which is consistent with the formation of hisingerite ($Fe_2^{3+}Si_2O_5(OH)_4{\cdot}2H_2O$ 1640 cm^{-1}) or a trioctahedral mineral such as stevensite (1638 cm^{-1}) or saponite (1630–1650 cm^{-1}), although this band occurs at a higher wave number than is generally recognized for these minerals.

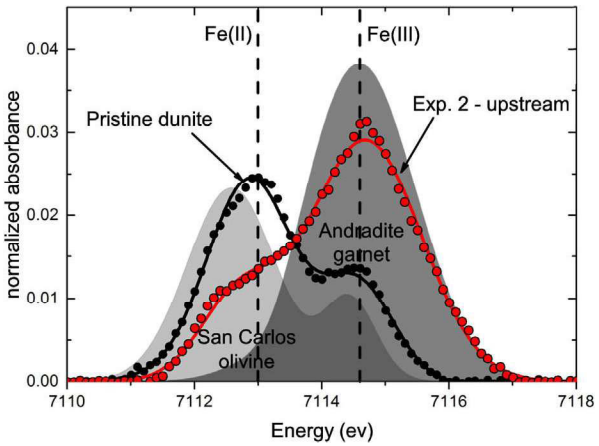

Fig. 12. Representative Fe K-edge XANES spectra (circles) and fits to these spectra (lines) of pristine and post-Experiment 2 samples compared with fitted Fe(II)- (San Carlos olivine) and Fe (III)- (andradite garnet) bearing model compounds (filled curves). The centroids of the Fe(II) and Fe(III) components, determined using these model compounds, are plotted as dashed lines. Although the post-Experiment 2 spectra necessarily show features representative of both olivine and alteration phases due to the comparatively large beam size (10 μm), the post-Experiment 2 spectra clearly show a shift towards increasing Fe(III) content. A summary of all XANES measurements is included in Table 8.

Table 8
Summary of Fe K-edge XANES measurements performed on model compounds and pristine and post-Experiment 2 samples.

Sample	Centroid	Integrated intensity	Number of spectra
San Carlos olivine	7113.0 ± 0.04	0.045 ± 0.005	3
Andradite garnet	7114.6 ± 0.08	0.111 ± 0.041	2
Pristine dunite	7113.3 ± 0.14	0.050 ± 0.006	4
Post-Exp. 2 dunite	7114.0 ± 0.29	0.068 ± 0.012	3

Based upon these considerations of our limited dataset, the alteration phases are most likely a mixture of serpentine, saponite, and talc. Since talc nominally accepts no Fe into its structure, it is likely that the serpentine phase contains the bulk of the oxidized Fe formed during the alteration process, although we cannot rule out that ferric Fe was incorporated into saponite.

XRCT scans indicated that pores in the dunite samples were so small that they could not be resolved with the XRCT resolution (Fig. 14). The presence of dense chromite grains in the cores facilitated alignment of pre- and post-experiment scans. Once aligned, we subtracted pre- from post-experimental XRCT data to highlight changes from fluid-rock reaction. However, neither XRCT dataset showed any change from fluid-rock reaction.

(U)SANS measurements on both post-experimental dunite samples produced scattering intensities that were generally higher than the intensities for the two pristine samples (Fig. 15). The scattering intensities for the core from Experiment 1 were generally higher than the intensities from the core from Experiment 2 at low Q

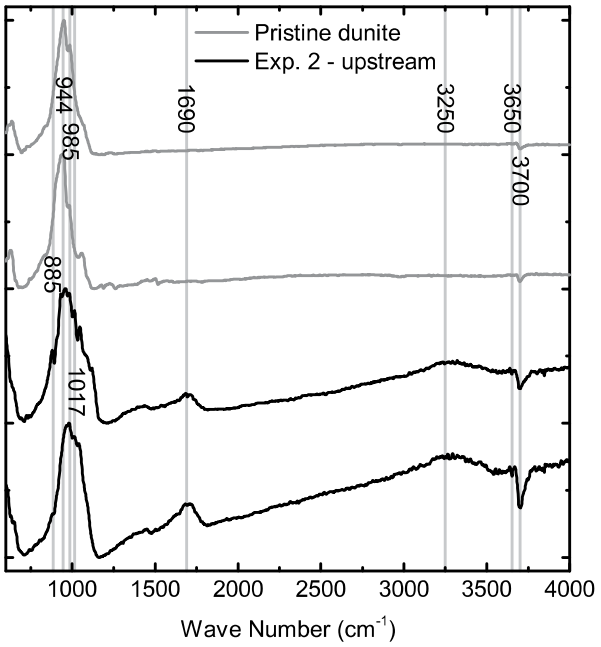

Fig. 13. FT-IR spectra collected near grain boundaries that illustrate experimental alteration. While spectra from the pristine dunite and the post-Experiment 2 dunite portray evidence of the dunite's primary mineralogy, the two spectra from the Experiment 2 sample also illustrate additional peaks indicative of secondary phases, likely additional serpentine, saponite, and talc.

($Q < \approx 0.012$ Å^{-1}), whereas the intensities were generally higher from Experiment 2 at high Q ($Q > \approx 0.012$ Å^{-1}). (U)SANS data are provided as Supplementary Data.

A Porod transform plot ($Q^4 \times I(Q)$ versus Q) illustrates slope variability in scattering data (Anovitz et al., 2009), highlighting a slope transition at $Q \approx 0.007$–0.009 Å^{-1} in our dunite dataset (Fig. 16). Fitting low Q scattering data below this transition indicates a surface fractal for all four samples (Table 9), where the values of n for the pristine samples and the core from Experiment 2 range from 3.50 to 3.54. The value of n for the core from Experiment 1 is 3.59. In contrast, the values of n at higher Q (i.e., generally $Q > 0.007$–0.009 Å^{-1}) are 2.81 and 2.82 for the pristine samples and 2.86 for the cores from Experiments 1 and 2, and thus, indicative of mass fractals (Table 9). Previous research on igneous rocks has identified mass fractals at low Q and surface fractals at high Q (Navarre-Sitchler et al., 2013, 2015; Bazilevskaya et al., 2015) or surface fractals at low Q and nonfractal at high Q (Luhmann et al., 2017b).

Calculated porosity from (U)SANS analyses yielded the largest value for the core from Experiment 1 and the smallest value for one of the pristine samples (Table 9). Porosity for the other pristine dunite sample was similar to the value calculated for the core from Experiment 2. The range of (U)SANS porosity calculations was larger with lower and higher values than the two post-experimental core connected porosity measurements (Table 2). Similarly, the SSA of the core from Experiment 1 was generally higher than the other three samples across the entire scatterer radius range (Fig. 17). The SSA of the core from Experiment 2 was generally slightly higher than the two pristine samples. Finally, the SSA extrapolation to 4 Å was 2.6–2.7 m^2/g for all four samples, with no discernable trend with experimental alteration.

4. DISCUSSION

4.1. Rock physical properties and permeability changes

The water saturation measurements and (U)SANS calculations yielded similar porosity values, with the (U)SANS data providing a larger range in porosity as well as smaller and larger values (Tables 2 and 9). As neutrons penetrate the entire sample, they measure both connected and unconnected porosity (including, for example, fluid inclusions), whereas the water saturation measurements solely record connected porosity. Still, the similarity in porosity values between the two methods suggests that most of the porosity is connected, although the slightly higher (U)SANS porosity calculations for the sample from Experiment 1 may suggest that disconnected pores are present. As both porosity methods provided relatively low values (ranging from 2.1% to 4.3%) and no porosity was visible with the XRCT resolution (Fig. 14), little porosity change in the dunite could reduce porosity below a critical threshold and make the samples effectively impermeable.

(U)SANS porosity measurements generally fell within the range of previously reported (U)SANS porosity measurements of partially serpentinized, olivine-rich samples (Tutolo et al., 2016). In their analysis of olivine-rich samples from the Atlantis Massif near the Mid-Atlantic Ridge and the Duluth Complex from the Mid-Continent Rift of North America, Tutolo et al. (2016) conducted (U)SANS analyses of samples much more altered than those reported here. Still, they noted an increase in SSA with alteration, with values that ranged from 0.08 to 0.4 m^2/g for zones that had undergone relatively little serpentinization to 2–14 m^2/g for regions where serpentinization was more significant. Using BET analyses, Okland et al. (2014) also noted an increase in SSA with alteration, with values of 1.7, 3.2, and 7.1 m^2/g for unaltered, medium altered, and highly altered dunite, respectively, from Norway. Our results are consistent with these previous studies, as both the pristine and post-experimental samples, all with relatively little alteration, are characterized by a relatively low SSA (2.6–2.7 m^2/g) (Table 9).

Permeability decreased for both experiments, but the permeability decrease during Experiment 2 was an order of magnitude more than during the lower temperature experiment (Fig. 4 and Table 2). Still, even with the permeability reduction of 25 times in Experiment 2, there was no observable change from the pre- to post-experimental XRCT scans, indicating that permeability changes occurred at length scales below the 8 μm voxel resolution of the XRCT. Furthermore, while the core from Experiment 1 generally yielded the largest intensities, porosities, and surface areas from (U)SANS analyses (Figs. 15 and 17 and Table 9), Experiment 2 produced much larger changes in dissolved gas and fluid chemistry (Tables 3 and 4), indicat-

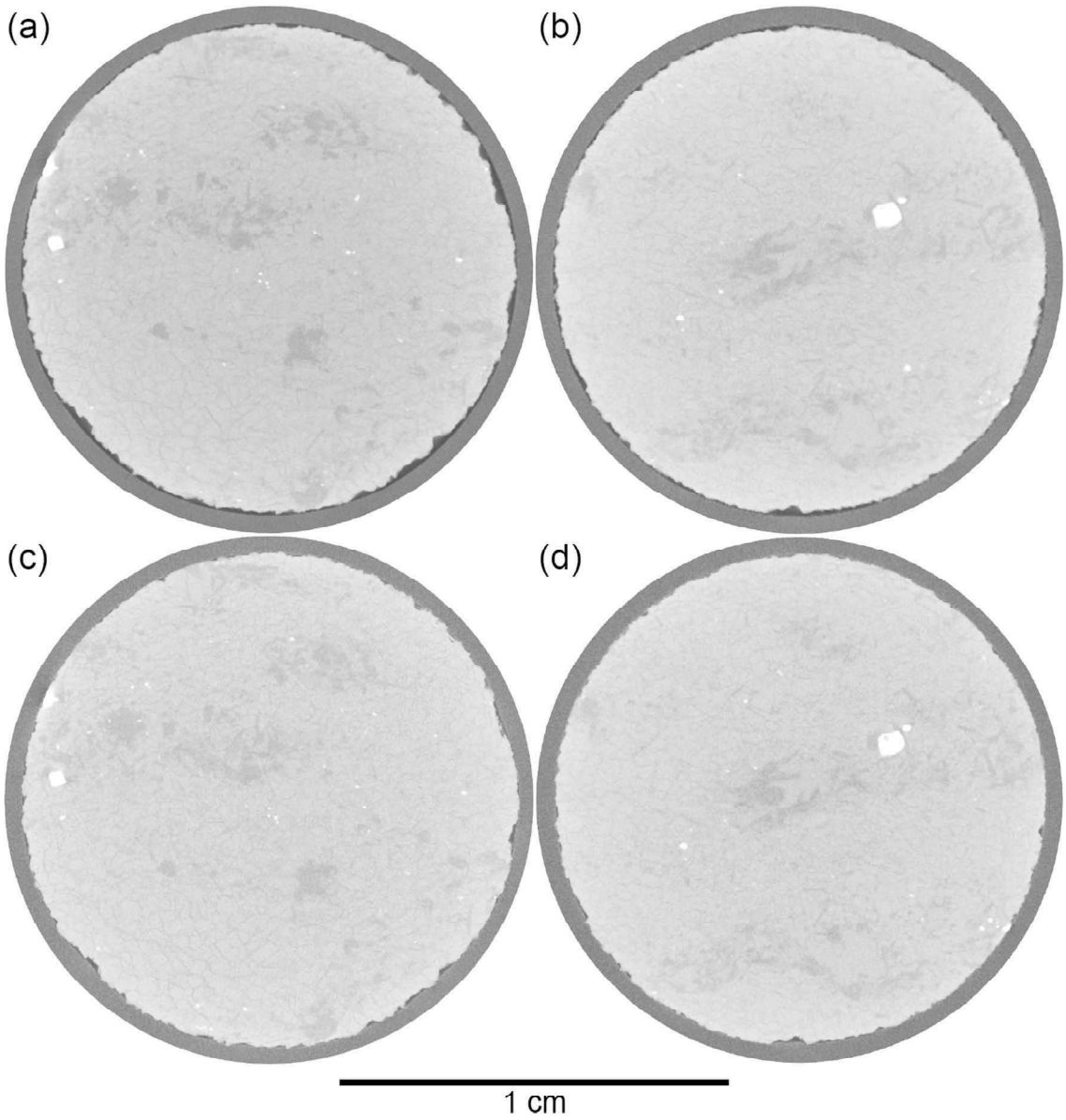

Fig. 14. XRCT cross-sectional pictures of the (a and b) pre- and (c and d) post-experimental core from Experiment 2, illustrating negligible change near the ends of the core. The pictures portray about half of the Teflon sheath surrounding the core.

ing significantly more reaction. Therefore, that the (U)SANS porosity and surface area for the core from Experiment 2 fell within the range of the values for the core from Experiment 1 and the pristine samples suggests that any change in porosity and surface area over the ≈1 nm- to 10 μm-scale range was within the range of the natural variability of the dunite sample. Furthermore, experimental alteration caused negligible change in fractal characteristics (provided by (U)SANS analyses), as similar fractal dimensions were determined for the pristine and post-experimental reacted samples (Table 9). Still, even with little to no reaction as suggested by XRCT and (U)SANS analyses, this limited reaction in small pores was sufficient to produce a significant decrease in permeability. SEM images revealed ≈1 μm honeycomb-textured secondary mineralization and larger calcite rhombs (Fig. 9). EDS analyses indicated additional serpentine formation with Cl uptake (Table 5), and FT-IR analyses suggested formation of additional serpentine, saponite, and talc (Fig. 13). Due to their voluminous nature, these minerals, while overall accounting for a relatively small proportion of the core, can have a dramatic effect on core permeability, especially in the dunite sample with very low porosity (Tables 2 and 9). As secondary phases precipitate in small pore throats, the newly-formed minerals can reduce permeability by reducing the hydraulic radius of the pore throat or increasing tortuosity (Gouze and Luquot, 2011) and roughness.

The significant permeability reduction during Experiment 2 is in agreement with previously reported experiments. Farough et al. (2016) observed permeability

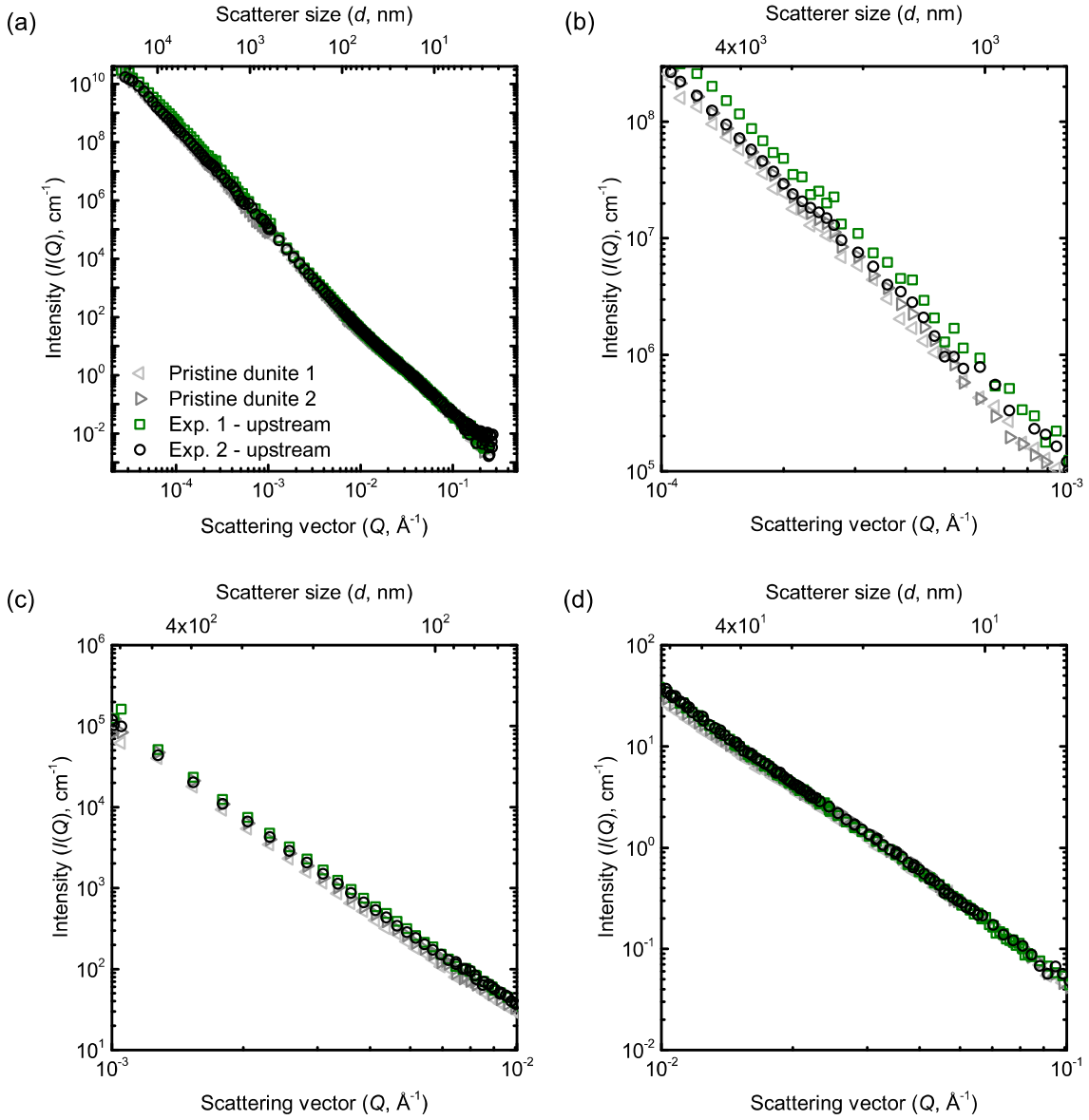

Fig. 15. Scattering curves for sections of the post-experimental cores from Experiments 1 and 2 and two pristine dunite samples. The scattering vector, Q, is associated with a real space distance, d, given by $d \approx 2\pi/Q$. Scattering intensities of both post-experimental dunite samples were higher than the values for the two pristine samples. The entire scattering curve is shown in (a), and (b–d) are focused on smaller portions of the curve.

decreases more than two orders of magnitude while flowing deionized water through crushed ultramafic rock and fractured ultramafic rock cores for 200–330 h at 260 °C. Following the experiments, they noted chemical analyses of alteration products that were consistent with serpentine mineralization and concluded that long-term flow through ultramafic-hosted hydrothermal systems requires tectonic activity and crystallization pressure to counter plugging in fractures from serpentine precipitation. While flowing seawater through sintered olivine cores at 190 °C and 19 MPa, Godard et al. (2013) observed a permeability decrease of more than one order of magnitude during an experiment that lasted 23 days. Godard et al. (2013) employed two flow rates that were one third and one order of magnitude lower than the flow rate used in our experiments, and they injected a volume that was nearly an order of magnitude lower than those reported here into their 9 mm diameter by 18 mm long core. Whereas our initial seawater had a Si concentration of 1.63 mmol/kg and essentially no Mg, the seawater of Godard et al. (2013) had significant dissolved Mg (41 mmol/kg) and minor Si (0.15 mmol/kg). They observed larger outlet fluid chemical changes, where Mg was consumed by secondary mineralization to yield outlet concentrations of 37–39 mmol/kg and Si rose from dissolution to 8.0–11.5 mmol/kg. In contrast, outlet Mg concentrations generally increased to 0.2 mmol/kg during Experiment 2 and dissolved Si was generally consumed by precipitation to produce values around 1 mmol/

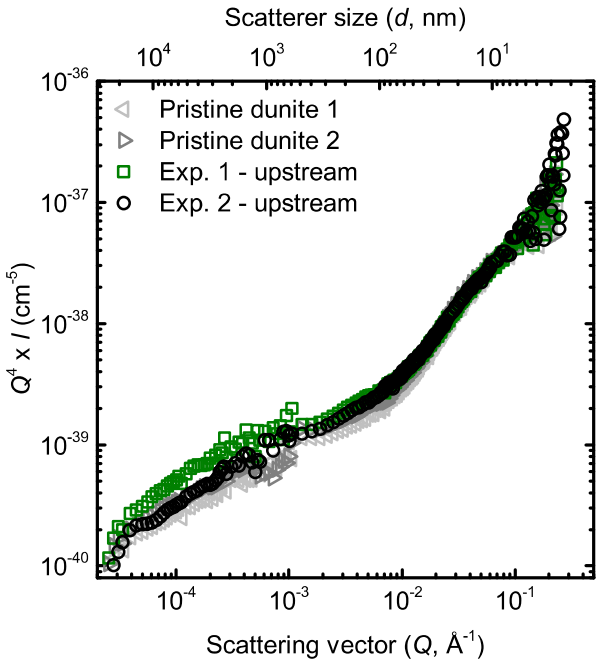

Fig. 16. The Porod transform plot ($Q^4 \times I(Q)$ versus Q) (Anovitz et al., 2009) accentuates slope changes in (U)SANS data. Trends in this figure and fitting of the data in Fig. 15 indicate surface fractals for all four samples at low Q and mass fractals for all four samples at high Q, with the transition occurring at $Q \approx 0.007$–0.009 Å^{-1}.

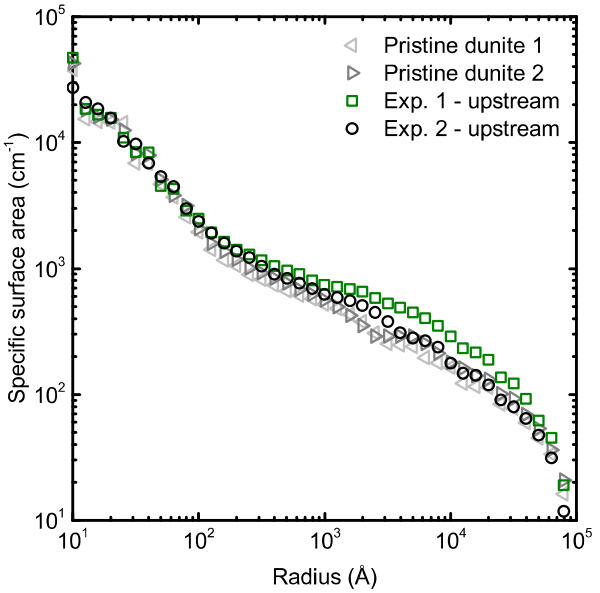

Fig. 17. Specific surface area (SSA) as a function of radius for sections of the post-experimental cores from Experiments 1 and 2 and two pristine dunite samples. The SSA of the core from Experiment 2 was generally within the range of values for the two pristine samples and the core from Experiment 1 across the entire radius range.

kg outside of the brief increase. At most, Godard et al. (2013) reported a max porosity change of 4.2%; with the order of magnitude decrease in permeability, they concluded that the permeability decrease was primarily caused by a reduction in the effective pore diameter and a tortuosity increase. The minor changes in core mass, XRCT, and (U)SANS datasets reported here suggest minor changes in porosity, but ultimately, secondary mineralization was significant enough to plug up pore throats and/or increase flow path tortuosity, with significant implications for the flow fields through the core.

4.2. Aqueous chemistry – dissolved solids

Outside of the early stage increase in dissolved Si, Si was generally lower than the starting solution concentration in Experiment 2 (Fig. 6 and Table 3). As olivine is converted to chrysotile and/or talc, dissolved Si would decrease (e.g., see Reaction (13) below). However, precipitation of chrysotile and/or talc was sufficiently sluggish so as not to fully consume the dissolved Si in the experimental solution.

Table 9
Calculated porosity, specific surface area (SSA), and Porod exponent (n) from (U)SANS data.

	Invariant – measured range porosity (%)	Invariant – extrapolation porosity (%)	PRINSAS porosity (%)	SSA at radius of 4 Å[a] (m^2/g)	n at low Q[b]	95% Confidence Interval	n at high Q[c]	95% Confidence interval
Pristine dunite 1	2.10	2.66	2.49	2.7	3.52	3.51–3.54	2.81	2.79–2.83
Pristine dunite 2	2.55	3.21	2.87	2.6	3.54	3.52–3.55	2.82	2.80–2.84
Post-Exp. 1	3.68	4.34	3.91	2.6	3.59	3.57–3.61	2.86	2.84–2.87
Post-Exp. 2	2.59	3.34	2.88	2.7	3.50	3.48–3.51	2.86	2.85–2.87

[a] Fit data in the range 15 Å < radius < 80 Å.
[b] Fits used the following ranges in Q: 5.08×10^{-5} Å^{-1}<Q< 6.78×10^{-3} Å^{-1} with an $R^2 = 1.000$ for the fit (Pristine dunite 1); 4.47×10^{-5} Å^{-1}<Q< 7.357×10^{-3} Å^{-1} with an $R^2 = 1.000$ for the fit (Pristine dunite 2); 4.46×10^{-5} Å^{-1}<Q< 8.511×10^{-3} Å^{-1} with an $R^2 = 1.000$ for the fit (Post-Exp. 1); 5.0×10^{-5} Å^{-1}<Q< 8.684×10^{-3} Å^{-1} with an $R^2 = 1.000$ for the fit (Post-Exp. 2).
[c] Fits used the following ranges in Q: 7.069×10^{-3} Å^{-1}<Q< 1.410×10^{-1} Å^{-1} with an $R^2 = 0.998$ for the fit (Pristine dunite 1); 7.473×10^{-3} Å^{-1}<Q< 1.293×10^{-1} Å^{-1} with an $R^2 = 0.999$ for the fit (Pristine dunite 2); 8.684×10^{-3} Å^{-1}<Q< 8.181×10^{-2} Å^{-1} with an $R^2 = 0.999$ for the fit (Post-Exp. 1); 8.799×10^{-3} Å^{-1}<Q< 1.293×10^{-1} Å^{-1} with an $R^2 = 0.999$ for the fit (Post-Exp. 2).

Wollastonite precipitated in the upstream portion of the reaction cell (Fig. 11) while at experimental temperature (due to decrease in solubility with increasing temperature) via the following reaction:

$$SiO_2(aq) + Ca^{2+} + H_2O = CaSiO_3 + 2H^+. \quad (7)$$

The precipitation of this phase had an effect on the decrease in outlet dissolved Si, but it could account for only a small fraction of the observed decrease. Precipitation of chrysotile and/or talc more likely accounts for most of the decrease in dissolved Si. Malvoisin et al. (2012c) noted that wollastonite can form at low temperatures under reducing conditions. While the wollastonite formed in the upstream piston assembly before Fe oxidation in the core, it likely formed with O_2 concentrations of ≈0.2 ppm, following attempts to purge O_2 from all solutions with N_2 gas (Butler et al., 1994).

Orthopyroxene was observed in thin section, and dissolution of orthopyroxene could increase dissolved Si and account for the brief, elevated Si concentration in the samples collected at 4.66 and 6.65 days (Fig. 6 and Table 3). This would occur as enstatite is altered to serpentine:

$$MgSiO_3 + 0.67H_2O = 0.33Mg_3Si_2O_5(OH)_4 + 0.33SiO_2(aq), \quad (8)$$

where dissolution of enstatite releases Si to solution faster than it is consumed by secondary phases (Seyfried and Dibble, 1980; Janecky and Seyfried, 1986; Allen and Seyfried, 2003). The transient increase potentially indicates time-dependent access to surface area that facilitates fluid-rock reaction as flow paths open to Si-rich sources. Alternatively, the increase in Si could have resulted from dissolution of a Si-rich metastable phase that precipitated during the early stage of reaction, such as wollastonite (Fig. 11), which was near saturation throughout the experiment (Fig. 7). Experimental data do not allow us to fully constrain the source of the elevated Si concentration, but the dissolved Si time series documents transient behavior during the initial stages of serpentinization.

The small Ca decrease (Table 3) was likely largely controlled by the precipitation of calcite noted on the downstream portion of the core (Fig. 9d) as well as the wollastonite identified in the upstream piston assembly (Fig. 11). We cannot rule out the possibility that the small Ca decrease was due to tremolite formation, which was highly supersaturated (Fig. 7) and is commonly observed with serpentine in altered ultramafic rocks affected by Si metasomatism at a wide range of temperatures (Frost and Beard, 2007). In this case, Ca would be consumed as forsterite is altered to tremolite:

$$Mg_2SiO_4 + 1.2H_2O + 2.2SiO_2(aq) + 0.8Ca^{2+} = 0.4Ca_2Mg_5Si_8O_{22}(OH)_2 + 1.6H^+. \quad (9)$$

All fluid samples from Experiment 2 plot in the chrysotile field on an activity-activity diagram for the MgO-SiO_2-H_2O-HCl system (Fig. 18). The clustering of the samples in the chrysotile field of stability expresses more about the relative rates of reaction than it does overall mineral stability. Indeed, the observation that the fluid chemistry is stationary within the activity space in the MgO-SiO_2-H_2O-HCl system suggests that a balance has been achieved between the rate of olivine dissolution and the rate of precipitation of hydrous secondary minerals. Clearly, the limited reactive surface area and relatively short residence time of fluid in the core precluded efficient and complete Si uptake by olivine hydrolysis and serpentine and/or talc formation. Given sufficient surface area and residence time, fluid chemistry in activity space would move away from the forsterite field of stability and plot along serpentine-fluid (SiO_2(aq)) or talc-fluid (SiO_2(aq)) phase boundaries. This condition has not been achieved, and thus, because olivine is continuously reacting, hydrous phases like chrysotile and talc were supersaturated throughout the experiment. Nesbitt and Bricker (1978) reported on fluids emerging from dunites and peridotites in nature that were in equilibrium with forsterite, which occurred in a dissolution-controlled environment where dissolution of the anhydrous minerals was much faster than hydrous mineral precipitation. Janecky and Seyfried (1986) reacted peridotites with seawater solutions at 200 °C and 300 °C, producing fluids that indicated a range of responses between precipitation and dissolution-controlled reactions.

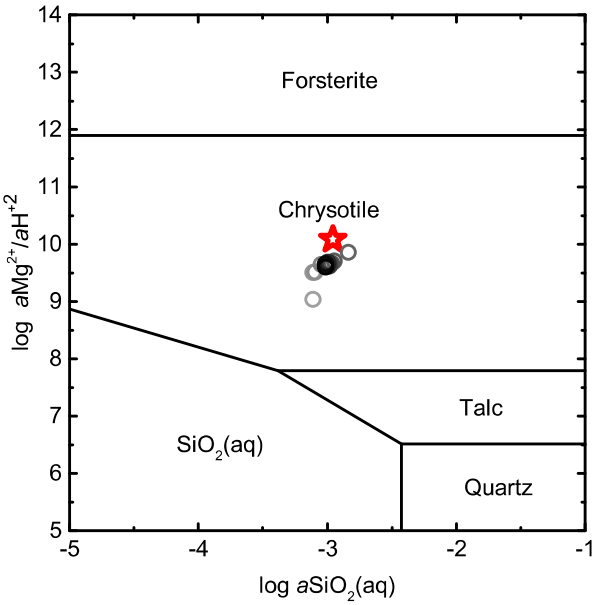

Fig. 18. Activity-activity diagram illustrating equilibrium for the MgO-SiO_2-H_2O-HCl system at 200 °C and 150 bar. The initial fluid (denoted by the red star) and outlet samples (denoted by grayscale to indicate relative time; light gray and black indicate beginning and end of experiment, respectively; 3 diluted samples with lower Na concentrations are not included) collected during Experiment 2 plot in the chrysotile field. The residence time of the experimental fluid was insufficient to develop equilibrium with any mineral phase. (For interpretation of the references to color in this figure legend, the reader is referred to the web version of this article.)

4.3. Aqueous chemistry – dissolved gases

The two experiments produced a significant difference in dissolved H_2 and CH_4 (Table 4). While Experiment 2

employed an evolved seawater that was rich in Si, it is likely that the higher temperature (200 °C vs 150 °C) is largely responsible for the one to two orders of magnitude increase in H_2 and CH_4, respectively. The H_2 concentrations were similar for Experiment 1 and the blank experiment, but since Experiment 1 was conducted at 150 °C while the blank experiment was run at 200 °C, it is problematic to identify if the H_2 during Experiment 1 resulted from reaction with the dunite core or the experimental apparatus.

4.3.1. CH_4

One potential source of CH_4 generation occurs via Fischer–Tropsch type reactions, where hydrocarbons are produced abiotically (Berndt et al., 1996; Horita and Berndt, 1999; McCollom and Seewald, 2001; Foustoukos and Seyfried, 2004; Proskurowski et al., 2008). For example, CH_4 can be produced in H_2-rich environments as aqueous CO_2 is reduced via the following reaction:

$$CO_2(aq) + 4H_2(aq) \rightarrow CH_4(aq) + 2H_2O. \quad (10)$$

However, McCollom and Seewald (2001) and McCollom (2016) noted that in the absence of mineral catalysts or a separate H_2-rich vapor phase, little CH_4 is produced by Reaction (10) over experimental timescales. Alternatively, dissolved CH_4 could arise from fluid interacting with organic material on grain surfaces. Organic compounds have been identified on olivine crack surfaces, with the organics likely originating during the time of thermal stresses associated with eruption and cooling of basalts and peridotite xenoliths (Tingle et al., 1990, 1991; Tingle and Hochella, 1993). The CH_4 concentration continually increased throughout Experiment 2 (Fig. 8), and the increase was potentially either caused by CH_4 diffusion through the Teflon into the confining fluid (where rising concentrations in the confining fluid from initial diffusion would limit subsequent diffusion, and thus, increase concentrations in the pore fluid) or experimental fluid accessing more organic material in the core with time as reaction opened new flow paths. Finally, fluid inclusions have been invoked as a source of preexisting volatiles, where they can be incorporated in the fluid during a process that is largely independent of active serpentinization (Kelley, 1996; McDermott et al., 2015; Wang et al., 2016). Since linear bands of fluid inclusions were observed in thin section (Fig. 3) and olivine is distinguished by conchoidal fracture, the parallel, discontinuous, and linear dissolution features that were observed in thin section (Fig. 10c and d) likely arose from dissolution focused along bands with abundant fluid inclusions. Dissolution that reached these trapped gas features would have released CH_4 to solution if the fluid inclusions were CH_4-rich.

4.3.2. H_2 and ferric Fe-rich serpentine

Olivine is generally unstable near the Earth's surface and will convert to Mg-bearing hydrous secondary minerals in the presence of water (Beard et al., 2009; Kelemen and Hirth, 2012). At 200 °C, thermodynamic modeling suggests that Fo_{90} ($(Mg_{0.9}Fe_{0.1})_2SiO_4$) will react fully to serpentine and brucite and produce H_2 concentrations of ≈140 mmol/kg with water-to-rock mass ratios near unity (Klein et al., 2013). Even with the predictable thermodynamic drive for olivine dissolution, the combination of limited surface area and residence time led to relatively little olivine dissolution during the experiment (based on thin section microscopy, XRCT, SEM images, and (U)SANS measurements). Nevertheless, ≈240 μmol of H_2 were generated during the 200 °C experiment, calculated using the following integral:

$$A_{H_2}(t) = Q_m \int_{t'=0}^{t'=t} C_{H_2}(t')dt', \quad (11)$$

where A_{H_2} is the total amount of H_2 recovered in the outlet fluid, Q_m is the mass fluid flow rate, C_{H_2} is the outlet H_2 concentration, and t is time. This total H_2 production calculation is a minimum because it does not account for the H_2 that diffused into the confinement fluid. The H_2 generated is significant, indeed, in comparison with the models of Klein et al. (2013), which suggest a total H_2 production of 1.4 mmol upon complete serpentinization of a 10 g (i.e., approximate mass of one of our experimental cores) sample of Fo_{90}. That said, it is difficult to make comparisons between our experiments and the calculations of Klein et al. (2013) because of inherent differences between the two methodologies. Fe-brucite precipitated from Fo_{90} alteration at 200 °C in the model system described in Klein et al. (2013), whereas our continuous supply of Si-rich fluids precluded brucite formation.

Experiment 2 at 200 °C generated H_2 concentrations of ≈300–600 μmol/kg (Fig. 8 and Table 4). Because the H_2 concentrations during this experiment were an order of magnitude higher than the blank experiment, the H_2 generation is generally attributed to oxidation of Fe(II) in the olivine to Fe(III). Mayhew et al. (2013) identified a strong correlation between H_2 production and the presence of spinel phases in the initial mineral composition during experiments at 55 °C and 100 °C. They propose that the primary pathway for H_2 generation occurs during electron transfer from spinel particles to adsorbed water molecules or protons. Iron oxidized in this manner may arise from iron in the spinels directly or else aqueous Fe(II) that arises from the dissolution of primary Fe-bearing minerals (Mayhew et al., 2013). Perhaps a portion of the H_2 production during the experiments reported here was made possible by the presence of chromite in the experimental cores. Still, the dissolution bands indicate that H_2 was certainly produced from iron oxidation during olivine dissolution (Fig. 10c and d). Regardless, following an initial peak, dissolved H_2 decreased in concentration for most of Experiment 2 (Fig. 8), potentially suggesting alteration that further passivated already partly passivated olivine grains and limited subsequent reaction. One potential H_2-producing mechanism involves the conversion of olivine to magnetite and serpentine (chrysotile), as given in the following reaction:

$$(Mg_{0.9}Fe_{0.1})_2SiO_4 + 1.27H_2O + 0.2SiO_2(aq) = 0.067Fe_3O_4 + 0.6Mg_3Si_2O_5(OH)_4 + 0.067H_2(aq). \quad (12)$$

If all oxidized Fe from olivine dissolution is ultimately incorporated into magnetite, H_2 and magnetite would be produced in equal amounts on a molar basis. Thus, a minimum of ≈240 μmol of magnetite should have precipitated in the core since a minimum of ≈240 μmol of H_2 were generated if Reaction (12) was responsible for the H_2 generation. This is equivalent to ≈55 mg of magnetite. However, while the VSM measurements indicate a slight magnetite enrichment in the post-experimental core from Experiment 2 (Table 7), mass balance constraints suggest this enrichment is negligible, or a factor of 80 less than it should be given Reaction (12). Furthermore, as written, the reaction would require dissolution of ≈0.5 g of olivine (i.e., ≈5% of the total core mass), which seems unlikely since so little dissolution was observed. Thus, Reaction (12) cannot account for the H_2 production observed.

Although Klein et al. (2015) noted magnetite production during initial harzburgite serpentinization, previous research has generally noted a lack of magnetite during initial stages of serpentinization (Toft et al., 1990; Oufi et al., 2002; Bach et al., 2004, 2006; Beard et al., 2009; Evans et al., 2009; Frost et al., 2013; Miyoshi et al., 2014). Furthermore, Seyfried et al. (2007) and Lafay et al. (2012) have noted little to no production of magnetite during experimental serpentinization at temperatures ≤200 °C, a point which has been corroborated by serpentinized peridotites from the field (Klein et al., 2014). Our results are consistent with the previous studies and suggest temperature control on magnetite formation. Furthermore, Frost and Beard (2007) show that high Si stabilizes iron-rich serpentine, inhibiting magnetite formation.

Beard et al. (2009) and Frost et al. (2013) have noted that serpentine that forms during early stages of serpentinization is generally Fe-rich, although there are exceptions (Klein et al., 2015). Furthermore, significant ferric Fe can be incorporated into serpentine (Seyfried et al., 2007; Evans et al., 2009, 2013a). In this case, H_2 is produced as olivine is converted to ferric Fe serpentine. Evans et al. (2009, 2013a) discuss mechanisms whereby ferric Fe is incorporated into lizardite. One mechanism produces cronstedtite as one component in the serpentine structure, as is shown in the following reaction:

$$20(Mg_{0.9}Fe_{0.1})_2SiO_4 + 15H_2O + 29SiO_2(aq) = (Fe^{2+}_2Fe^{3+})(Fe^{3+}Si)O_5(OH)_4 + 12Mg_3Si_4O_{10}(OH)_2 + H_2(aq). \quad (13)$$

While it is difficult to constrain the specific serpentine structure produced in these experiments, H_2 was likely produced as ferrous Fe was oxidized to ferric Fe and incorporated into serpentine on the basis of the observed lack of magnetite.

Importantly, our experimental flow system represents an open system, which more closely approximates conditions in nature during active serpentinization of olivine. For example, Streit et al. (2012) identified hematite in serpentinized, carbonated peridotite from Oman, suggesting an open system with relatively high oxygen fugacity. Klein et al. (2013) noted that H_2 loss is likely in open systems, which subsequently facilitates additional oxidation of Fe, producing more magnetite and ferric Fe serpentine than would be possible in closed system environments, where reactions would no longer proceed and potentially reverse as H_2 becomes elevated. Natural systems frequently produce much lower H_2 concentrations (e.g., Kelley et al., 2001; Seyfried et al., 2015), due to open system dynamics. However, it is this H_2 loss that facilitates additional production that can lead to significantly more H_2 generation than would be possible in closed systems. For example, as an end-member, if H_2 is continually removed as fluid reactants are continually refreshed such that all ferrous Fe in olivine is oxidized to ferric Fe via the following general reaction

$$2FeO + H_2O = Fe_2O_3 + H_2(aq), \quad (14)$$

then altering 1 kg of Fo_{90} would produce 680 mmol of H_2, approximately five times larger than the closed system prediction of Klein et al. (2013). This would occur as ferric Fe is incorporated into lizardite via a vacancy-balanced substitution (Evans et al., 2009, 2013a); for example,

$$10(Mg_{0.9}Fe_{0.1})_2SiO_4 + 9H_2O + 16SiO_2(aq) = (\square Fe^{3+}_2)Si_2O_5(OH)_4 + 6Mg_3Si_4O_{10}(OH)_2 + H_2(aq). \quad (15)$$

This reaction is likely only stable in relatively low H_2 conditions. Even if half of the ferrous Fe is oxidized, as in Reaction (13), then altering 1 kg of Fo_{90} would produce 340 mmol of H_2. Therefore, an open system is more efficient at H_2 generation because the H_2 loss accommodates subsequent H_2 production, which essentially stabilizes ferric Fe-rich serpentine. Evans et al. (2013a) noted that lizardite contains abundant ferric Fe (typically 50–90% of the total Fe), such that whole-rock Fe^{3+}/Fe^{2+} ratios can be higher than the ratio in magnetite. This degree of ferric Fe in samples requires a history of significant H_2 generation, made possible by flowing fluids that prevent relatively high H_2 concentrations.

Based on the H_2 production during Experiment 2, Reaction (13) would require alteration of ≈0.71 g of Fo_{90} (congruent dissolution of olivine used here with less iron and a composition of Fo_{92} (Table 5) would require an even larger dissolved mass, especially given the minimum H_2 production calculation), which seems unlikely since no change was observed in the XRCT data, even though the resolution provided by the XRCT is not capable of resolving the thin linear dissolution bands portrayed in Fig. 10c and d. In addition, although the H_2 generating efficiency inherent to Reaction (15) requires much less olivine reaction (minimum estimate of 0.35 g of Fo_{90}), the predicted value is likely still in excess of that portrayed in SEM pictures of dissolution, especially since much of the thin section depicted less dissolution than shown in Fig. 10c. The forsterite component certainly dissolved, as indicated by the increase in dissolved Mg (Table 3). However, as suggested by the EDS spot analysis on the partially dissolved olivine that indicated more Fe removal than either Mg or Si (Table 5), the experimental solution may have preferentially reacted with the Fe-rich fayalite component of the olivine to alter a relatively small mass of the dunite core, and yet, produce significant H_2. As a non-ideal solid solution, the activity of fayalite could be

considerably greater than the mole fraction, with the corresponding effect of over expressing its capacity to leave the olivine solution while providing H_2 to the aqueous solution and altering to serpentine. The ion activity product (and Fe concentrations) for a fluid in contact with the olivine solid solution would be less than expected if the fluid was in equilibrium with a pure fayalite phase (Stumm and Morgan, 1996; Brezonik and Arnold, 2011). However, the low measured Fe concentrations (to the extent of several samples being below the detection limit, Table 3) ensured a strong thermodynamic drive for reaction of the fayalite component.

Furthermore, and perhaps even more importantly, the kinetics of forsterite and fayalite dissolution likely contribute to incongruent olivine dissolution. Kinetic experiments at lower temperatures have demonstrated that dissolution rates of fayalitic olivine are generally faster than forsterite dissolution rates (Wogelius and Walther, 1992), so perhaps the fayalite component in the solid solution dissolves faster than the forsterite component. In addition, Daval et al. (2010) noted that far-from-equilibrium dissolution rates for fayalite are about one order of magnitude faster than forsterite rates, although it is worth noting that their fayalite dissolution experiments were conducted under acidic conditions. While dissolved Fe^{3+} decreases fayalite dissolution rates (Santelli et al., 2001), precipitation of ferric Fe-rich serpentine necessarily maintained low dissolved Fe^{3+}, preserving a strong kinetic drive for fayalite dissolution. Previous research has generally noted that preferential elemental release does not result from nonstoichiometric dissolution, but rather, stoichiometric dissolution followed by secondary phase precipitation (e.g., Putnis, 2009; Ruiz-Agudo et al. 2012, 2014; Hellmann et al., 2012). At the same time, preferential release of minor elements has been documented, indicating that minor components may undergo nonstoichiometric dissolution (e.g., Luhmann et al. 2014). Future research will have to constrain whether it is indeed possible for nonstoichiometric dissolution of a minor component in a solid solution.

Additionally, FeMg diffusion in olivine is an incredibly slow process (Evans, 2010), such that Fe cannot overexpress itself beyond olivine surfaces (Evans, 2010). The volume of a unit cell (with four formula units) of olivine is 290 $Å^3$ (Nesse, 2000). If the surface of the olivine is limited to the thickness of the unit cell (i.e., 4.75–10.20 Å; Nesse, 2000), then ≈0.004% of the unit cells in a cube with a side of ≈100 μm (i.e., approximately the length of the smallest olivine crystals in Fig. 2) would be present at the surface. With an olivine composition of Fo_{90}, conversion of all of the ferrous Fe in the unit cells at the surface to ferric Fe via Reaction (14) would produce ≈0.1% of the H_2 that was generated during Experiment 2. Grain surfaces are generally rough, and White and Peterson (1990) noted that rough surfaces increase surface area by an average factor of seven. Even while accounting for all of the Fe on rough olivine surfaces (i.e., increasing hypothetical cube surface area by a factor of seven), surface area in the core is still more than two orders of magnitude too small to account for the H_2 generation during Experiment 2. Thus, if olivine alteration was solely responsible for generating the H_2, then the little evidence of alteration and the high H_2 production suggests a dense network of cracks or preferential flow paths (possibly along growth planes or lattice imperfections) within individual olivine crystals, where the experimental fluid was able to access and oxidize ≈4% of the total Fe in the olivine via grain and crack surfaces. Cracks are visible in thin section (Fig. 2), and (U)SANS data (Fig. 15) likely incorporate additional smaller cracks that are not even observable with optical microscopy. Indeed, no preferential flow paths or crack networks were observable between the fluid inclusions in thin section (Fig. 3), but they nevertheless must have existed to allow the fluid to penetrate and dissolve linear bands within the inner olivine crystal cores (Fig. 10c and d). Even if the post-experimental dissolution bands were not at all related to the preexisting bands of fluid inclusions, preexisting preferential channels must have existed for the dissolution band features to make their way through the interiors of olivine crystals. Otherwise, fluid would have become stagnant in newly created dissolution pits, where dissolution would have become limited by diffusion. Perhaps there were additional cracks or flow paths through individual crystals that facilitated further Fe oxidation, but ultimately underwent less dissolution so as not to produce observable changes in the SEM pictures. Cutting of the core for various post-experimental analyses revealed that the brown, oxidized color was present throughout individual grains and the entire core and not simply isolated to grain boundaries, suggesting the effectiveness of a crack network for significant iron oxidation. Thus, the combination of a number of factors (nonstoichiometric olivine dissolution, kinetics, and crack network) is likely responsible for the significant H_2 generation with little evidence of alteration.

Finally, besides Fe oxidation, the high H_2 production during Experiment 2 is potentially partly due to dissolution that opened fluid inclusions, making preexisting volatiles accessible. As the dissolution bands were much longer than individual fluid inclusions (Figs. 3 and 10c and d) and XANES analyses confirmed Fe oxidation (Fig. 12), olivine was certainly dissolved. Still, the linear dissolution bands within olivine crystals potentially formed where they did because of preexisting linear bands of fluid inclusions. Thus, if the fluid inclusions contained H_2, then the H_2 detected in outlet fluids was also sourced from the fluid inclusions as dissolution penetrated these trapped gas features. Still, additional research is needed to constrain the relative importance of fluid inclusions versus active serpentinization in the overall H_2 budget.

5. CONCLUSIONS

Experiments were conducted on intact dunite cores to simulate incipient stages of serpentinization. Artificial seawater-type solutions flowed through the cores at 150 and 200 °C. The higher temperature experiment produced H_2 and CH_4 concentrations that exceeded 600 μmol/kg and 300 μmol/kg, respectively, while relatively little reaction occurred during the lower temperature experiment, underscoring the importance of temperature on the direc-

tion and magnitude of mass transfer during olivine hydrolysis. While the specific reaction pathway for CH_4 was not identified, the generated H_2 during the 200 °C experiment was at least partly produced via the oxidation of iron as ferrous Fe olivine was converted to ferric Fe-rich serpentine and possibly saponite, since negligible magnetite was produced during the experiment. It is also possible that H_2 concentrations in the fluid increased as dissolution made dissolved gases in fluid inclusions accessible. Dissolved Si was either below or above the starting solution composition during the 200 °C experiment, likely due to the formation of serpentine and/or talc and the dissolution of orthopyroxene, respectively. Dissolved Ca decreased slightly upon passing through the core during this experiment due to the formation of calcite, wollastonite, and/or tremolite. Secondary mineralization was observed on the post-experimental core from the 200 °C experiment. Still, even at a relatively low flow rate and a moderately high temperature, rates of secondary mineral formation were inefficient and not able to overcome olivine dissolution effects and achieve saturation, as fluids were still poised for secondary mineralization upon exiting the core. Furthermore, no significant change was observed from XRCT and (U)SANS datasets, indicating that relatively low levels of reaction can cause a significant permeability reduction (a factor of 25) in the low-porosity dunite sample, likely caused by secondary mineralization in key locations that reduced the hydraulic radius of pore throats or increased flow path tortuosity or roughness.

Fe is generally a minor component in the olivine mineral structure. Still, experimental results suggest relatively high fayalite reactivity, likely resulting from the combination of chemical and physical factors that include activities in the olivine solid solution, dissolution kinetics of forsterite and fayalite, and a crack network that provides access to numerous olivine surfaces. Furthermore, oxidation of Fe during serpentinization facilitates H_2 production, which provides environments that are conducive to abiotic synthesis of organic compounds, while also supporting biological communities independent of photosynthesis (McCollom and Seewald, 2013). Serpentinization can proceed in a rock-dominated system, where fluid chemistry is controlled by mineral components (Beard et al., 2009; Evans et al., 2013b; Frost et al., 2013). However, serpentinization in natural systems often occurs as fluids flow through ultramafic rocks, where open systems continually refresh fluid reactants with concomitant effects on hydrothermal alteration processes. Limited residence time for fluid-rock interaction necessarily produces relatively low H_2 concentration due to sluggish reaction kinetics. However, as flow continually removes H_2 from the system, the thermodynamic drive for further oxidation of ferrous Fe and subsequent H_2 production is maintained. Because of this, more H_2 may be generated for a given amount of peridotite than would be possible in a closed system, where a rising H_2 concentration would limit subsequent oxidation. This latter consideration can help to interpret field samples of partially serpentinized peridotites, such that the abundance of ferric Fe minerals can be suggestive of water-to-rock ratios that the rock has experienced in its past. Evans et al. (2013a) noted that Fe^{3+}/Fe^{2+} ratios in whole rocks are frequently higher than the ratio in magnetite. This is likely only possible because of open system dynamics, where systems contain ferric Fe serpentine and Fe^{3+}/Fe^{2+} ratios that are buffered more by the fluid than the rock.tpb 2

ACKNOWLEDGEMENTS

We thank Rick Knurr for fluid and rock analyses, Adam Schaen for help with gas analyses, Chunyang Tan for creating Fig. 1b, Daniel Maxbauer for VSM analyses, Nicholas Seaton for SEM pictures and analyses, Mark Zimmerman for providing the dunite sample, Jesus Gomez-Velez for the R code that was used to fit the (U)SANS data, and the Diamond Light Source for access to beamline I18 (proposal number SP15947) that contributed to the results presented here. We also thank Frieder Klein, Benjamin Malvoisin, and an anonymous reviewer for thorough reviews that led to significant improvements in our manuscript. XRCT data and images were produced at the X-ray Computed Tomography Laboratory in the Department of Earth Sciences, University of Minnesota (UMN), which was funded by a UMN Infrastructure Investment Initiative Grant. Access to the small-angle neutron scattering instruments was provided by the Center for High Resolution Neutron Scattering, a partnership between the National Institute of Standards and Technology and the National Science Foundation under Agreement No. DMR-0944772. The identification of commercial products in this paper does not imply recommendation or endorsement by the National Institute of Standards and Technology, nor does it imply that the equipment used are necessarily the best available for the purpose. SEM images were taken in the Characterization Facility, University of Minnesota, a member of the NSF-funded Materials Research Facilities Network (www.mrfn.org) via the MRSEC program. The IRM is supported as a National Multiuser Facility through NSF-EAR Instrumentation and Facilities grant 1339505. Research support was provided by the National Science Foundation Grant OCE 1426695.

APPENDIX A. SUPPLEMENTARY MATERIAL

Supplementary data associated with this article can be found, in the online version, at http://dx.doi.org/10.1016/j.gca.2017.07.020.

REFERENCES

Allen D. E. and Seyfried, Jr., W. E. (2003) Compositional controls on vent fluids from ultramafic-hosted hydrothermal systems at mid-ocean ridges: An experimental study at 400 °C, 500 bars. *Geochim. Cosmochim. Acta* **67**(8), 1531–1542. http://dx.doi.org/10.1016/S0016-7037(02)01173-0.

Andreani M., Daniel I. and Pollet-Villard M. (2013a) Aluminum speeds up the hydrothermal alteration of olivine. *Am. Mineral.* **98**(10), 1738–1744. http://dx.doi.org/10.2138/am.2013.4469.

Andreani M., Muñoz M., Marcaillou C. and Delacour A. (2013b) μXANES study of iron redox state in serpentine during oceanic serpentinization. *Lithos* **178**, 70–83. http://dx.doi.org/10.1016/j.lithos.2013.04.008.

Anovitz L. M., Lynn G. W., Cole D. R., Rother G., Allard L. F., Hamilton W. A., Porcar L. and Kim M.-H. (2009) A new

approach to quantification of metamorphism using ultra-small and small angle neutron scattering. *Geochim. Cosmochim. Acta* **73**(24), 7303–7324. http://dx.doi.org/10.1016/j.gca.2009.07.040.

Anovitz L. M., Cole D. R., Rother G., Allard L. F., Jackson A. J. and Littrell K. C. (2013) Diagenetic changes in macro- to nano-scale porosity in the St. Peter Sandstone: An (ultra) small angle neutron scattering and backscattered electron imaging analysis. *Geochim. Cosmochim. Acta* **102**, 280–305. http://dx.doi.org/10.1016/j.gca.2012.07.035.

Bach W., Garrido C. J., Paulick H., Harvey J. and Rosner M. (2004) Seawater-peridotite interactions: first insights from ODP Leg 209, MAR 15°N. *Geochem. Geophy. Geosy.* **5**(9), Q09F26. http://dx.doi.org/10.1029/2004GC000744.

Bach W., Paulick H., Garrido C. J., Ildefonse B., Meurer W. P. and Humphris S. E. (2006) Unraveling the sequence of serpentinization reactions: petrography, mineral chemistry, and petrophysics of serpentinites from MAR 15°N (ODP Leg 209, Site 1274). *Geophys. Res. Lett.* **33**(13), L13306. http://dx.doi.org/10.1029/2006GL025681.

Bandura A. V. and Lvov S. N. (2006) The ionization constant of water over wide ranges of temperature and density. *J. Phys. Chem. Ref. Data* **35**(1), 15–30. http://dx.doi.org/10.1063/1.1928231.

Barker J. G., Glinka C. J., Moyer J. J., Kim M. H., Drews A. R. and Agamalian M. (2005) Design and performance of a thermal-neutron double-crystal diffractometer for USANS at NIST. *J. Appl. Crystallogr.* **38**, 1004–1011. http://dx.doi.org/10.1107/S0021889805032103.

Bazilevskaya E., Lebedeva M., Pavich M., Rother G., Parkinson D. Y., Cole D. and Brantley S. L. (2013) Where fast weathering creates thin regolith and slow weathering creates thick regolith. *Earth Surf. Proc. Land.* **38**(8), 847–858. http://dx.doi.org/10.1002/esp.3369.

Bazilevskaya E., Rother G., Mildner D. F. R., Pavich M., Cole D., Bhatt M. P., Jin L., Steefel C. I. and Brantley S. L. (2015) How oxidation and dissolution in diabase and granite control porosity during weathering. *Soil Sci. Soc. Am. J.* **79**(1), 55–73. http://dx.doi.org/10.2136/sssaj2014.04.0135.

Beard J. S., Frost B. R., Fryer P., McCaig A., Searle R., Ildefonse B., Zinin P. and Sharma S. K. (2009) Onset and progression of serpentinization and magnetite formation in olivine-rich troctolite from IODP Hole U1309D. *J. Petrol.* **50**(3), 1–17. http://dx.doi.org/10.1093/petrology/egp004.

Berndt M. E., Allen D. E. and Seyfried, Jr., W. E. (1996) Reduction of CO_2 during serpentinization of olivine at 300 °C and 500 bar. *Geology* **24**(4), 351–354.

Bethke C. M. and Yeakel S. (2015) *The Geochemist's Workbench® Release 10.0 Reaction Modeling Guide*. Aqueous Solutions, LLC, Champaign, IL.

Boschi C., Früh-Green G. L., Delacour A., Karson J. A. and Kelley D. S. (2006) Mass transfer and fluid flow during detachment faulting and development of an oceanic core complex, Atlantis Massif (MAR 30 °N). *Geochem. Geophy. Geosy.* **7**(1), Q01004. http://dx.doi.org/10.1029/2005GC001074.

Boschi C., Dini A., Früh-Green G. L. and Kelley D. S. (2008) Isotopic and element exchange during serpentinization and metasomatism at the Atlantis Massif (MAR 30°N): Insights from B and Sr isotope data. *Geochim. Cosmochim. Acta* **72**(7), 1801–1823. http://dx.doi.org/10.1016/j.gca.2008.01.013.

Brazelton W. J., Schrenk M. O., Kelley D. S. and Baross J. A. (2006) Methane-and sulfur-metabolizing microbial communities dominate the Lost City hydrothermal field ecosystem. *Appl. Environ. Microb.* **72**(9), 6257–6270. http://dx.doi.org/10.1128/AEM.00574-06.

Brezonik P. L. and Arnold W. A. (2011) *Water Chemistry: An Introduction to the Chemistry of Natural and Engineered Aquatic Systems*. Oxford University Press, New York.

Butler I. B., Schoonen M. A. A. and Rickard D. T. (1994) Removal of dissolved oxygen from water: A comparison of four common techniques. *Talanta* **41**(2), 211–215. http://dx.doi.org/10.1016/0039-9140(94)80110-X.

Charlou J. L., Donval J. P., Fouquet Y., Jean-Baptiste P. and Holm N. (2002) Geochemistry of high H_2 and CH_4 vent fluids issuing from ultramafic rocks at the Rainbow hydrothermal field (36 14′ N, MAR). *Chem. Geol.* **191**(4), 345–359. http://dx.doi.org/10.1016/S0009-2541(02)00134-1.

Choi S.-M., Barker J. G., Glinka C. J., Cheng Y. T. and Gammel P. L. (2000) Focusing cold neutrons with multiple biconcave lenses for small-angle neutron scattering. *J. Appl. Crystallogr.* **33**, 793–796. http://dx.doi.org/10.1107/S0021889800099799.

Chukanov N. V. (2014) *Infrared Spectra of Mineral Species: Extended Library*. Springer, Dordrecht, Netherlands.

Darcy H. P. G. (1856) *Les Fontaines Publiques de la Ville de Dijon (The Public Fountains of the City of Dijon)*. Dalmont, Paris.

Daval D., Testemale D., Recham N., Tarascon J.-M., Siebert J., Martinez I. and Guyot F. (2010) Fayalite (Fe_2SiO_4) dissolution kinetics determined by X-ray absorption spectroscopy. *Chem. Geol.* **275**(3–4), 161–175. http://dx.doi.org/10.1016/j.chemgeo.2010.05.005.

Escartín J., Hirth G. and Evans B. (2001) Strength of slightly serpentinized peridotites: Implications for the tectonics of oceanic lithosphere. *Geology* **29**(11), 1023–1026.

Evans B. W. (2010) Lizardite versus antigorite serpentinite: Magnetite, hydrogen, and life(?). *Geology* **38**(10), 879–882. http://dx.doi.org/10.1130/G31158.1.

Evans B. W., Kuehner S. M. and Chopelas A. (2009) Magnetite-free, yellow lizardite serpentinization of olivine websterite, Canyon Mountain complex, N.E. Oregon. *Am. Mineral.* **94**(11–12), 1731–1734. http://dx.doi.org/10.2138/am.2009.3301.

Evans B. W., Hattori K. and Baronnet A. (2013a) Serpentinite: What, why, where?. *Elements* **9** 99–106. http://dx.doi.org/10.2113/gselements.9.2.99.

Evans K. A., Powell R. and Frost B. R. (2013b) Using equilibrium thermodynamics in the study of metasomatic alteration, illustrated by an application to serpentinites. *Lithos* **168–169**, 67–84. http://dx.doi.org/10.1016/j.lithos.2013.01.016.

Farough A., Moore D. E., Lockner D. A. and Lowell R. P. (2016) Evolution of fracture permeability of ultramafic rocks undergoing serpentinization at hydrothermal conditions: An experimental study. *Geochem. Geophy. Geosy.* **17**(1), 44–55. http://dx.doi.org/10.1002/2015GC005973.

Flores G. E., Campbell J. H., Kirshtein J. D., Meneghin J., Podar M., Steinberg J. I., Seewald J. S., Tivey M. K., Voytek M. A., Yang Z. K. and Reysenbach A.-L. (2011) Microbial community structure of hydrothermal deposits from geochemically different vent fields along the Mid-Atlantic Ridge. *Environ. Microbiol.* **13**(8), 2158–2171. http://dx.doi.org/10.1111/j.1462-2920.2011.02463.x.

Foustoukos D. I. and Seyfried, Jr., W. E. (2004) Hydrocarbons in hydrothermal vent fluids: The role of chromium-bearing catalysts. *Science* **304**(5673), 1002–1005. http://dx.doi.org/10.1126/science.1096033.

Foustoukos D. I., Savov I. P. and Janecky D. R. (2008) Chemical and isotopic constraints on water/rock interactions at the Lost City hydrothermal field, 30°N Mid-Atlantic Ridge. *Geochim. Cosmochim. Acta* **72**(22), 5457–5474. http://dx.doi.org/10.1016/j.gca.2008.07.035.

Frost B. R. and Beard J. S. (2007) On silica activity and serpentinization. *J. Petrol.* **48**(7), 1351–1368. http://dx.doi.org/10.1093/petrology/egm021.

Frost B. R., Evans K. A., Swapp S. M., Beard J. S. and Mothersole F. E. (2013) The process of serpentinization in dunite from New Caledonia. *Lithos* **178**, 24–39. http://dx.doi.org/10.1016/j.lithos.2013.02.002.

Früh-Green G. L., Kelley D. S., Bernasconi S. M., Karson J. A., Ludwig K. A., Butterfield D. A., Boschi C. and Proskurowski G. (2003) 30,000 years of hydrothermal activity at the Lost City vent field. *Science* **301**(5632), 495–498. http://dx.doi.org/10.1126/science.1085582.

Glinka C. J., Barker J. G., Hammouda B., Krueger S., Moyer J. J. and Orts W. J. (1998) The 30 m small-angle neutron scattering instruments at the National Institute of Standards and Technology. *J. Appl. Crystallogr.* **31**, 430–445. http://dx.doi.org/10.1107/S0021889897017020.

Godard M., Luquot L., Andreani M. and Gouze P. (2013) Incipient hydration of mantle lithosphere at ridges: A reactive-percolation experiment. *Earth Planet. Sc. Lett.* **371–372**, 92–102. http://dx.doi.org/10.1016/j.epsl.2013.03.052.

Gouze P. and Luquot L. (2011) X-ray microtomography characterization of porosity, permeability and reactive surface changes during dissolution. *J. Contam. Hydrol.* **120–121**, 45–55. http://dx.doi.org/10.1016/j.jconhyd.2010.07.004.

Guillot S. and Hattori K. (2013) Serpentinites: Essential roles in geodynamics, arc volcanism, sustainable development, and the origin of life. *Elements* **9**(2), 95–98. http://dx.doi.org/10.2113/gselements.9.2.95.

Hellmann R., Wirth R., Daval D., Barnes J.-P., Penisson J.-M., Tisserand D., Epicier T., Florin B. and Hervig R. L. (2012) Unifying natural and laboratory chemical weathering with interfacial dissolution–reprecipitation: A study based on the nanometer-scale chemistry of fluid–silicate interfaces. *Chem. Geol.* **294–295**, 203–216. http://dx.doi.org/10.1016/j.chemgeo.2011.12.002.

Hinde A. L. (2004) PRINSAS – a Windows-based computer program for the processing and interpretation of small-angle scattering data tailored to the analysis of sedimentary rocks. *J. Appl. Crystallogr.* **37**, 1020–1024. http://dx.doi.org/10.1107/S0021889804021260.

Horita J. and Berndt M. E. (1999) Abiogenic methane formation and isotopic fractionation under hydrothermal conditions. *Science* **285**(5430), 1055–1057. http://dx.doi.org/10.1126/science.285.5430.1055.

Jackson M. and Solheid P. (2010) On the quantitative analysis and evaluation of magnetic hysteresis data. *Geochem. Geophy. Geosy.* **11**(4), Q04Z15. http://dx.doi.org/10.1029/2009GC002932.

Janecky D. R. and Seyfried, Jr., W. E. (1986) Hydrothermal serpentinization of peridotite within the oceanic crust: Experimental investigations of mineralogy and major element chemistry. *Geochim. Cosmochim. Acta* **50**(7), 1357–1378. http://dx.doi.org/10.1016/0016-7037(86)90311-X.

Jin L., Rother G., Cole D. R., Mildner D. F. R., Duffy C. J. and Brantley S. L. (2011) Characterization of deep weathering and nanoporosity development in shale—A neutron study. *Am. Mineral.* **96**(4), 498–512. http://dx.doi.org/10.2138/am.2011.3598.

Kelemen P. B. and Hirth G. (2012) Reaction-driven cracking during retrograde metamorphism: Olivine hydration and carbonation. *Earth Planet. Sci. Lett.* **345–348**, 81–89. http://dx.doi.org/10.1016/j.epsl.2012.06.018.

Kelley D. S. (1996) Methane-rich fluids in the oceanic crust. *J. Geophys. Res.-Sol. Ea.* **101**(B2), 2943–2962. http://dx.doi.org/10.1029/95JB02252.

Kelley D. S., Karson J. A., Blackman D. K., Früh-Green G. L., Butterfield D. A., Lilley M. D., Olson E. J., Schrenk M. O., Roe K. K., Lebon G. T. and Rivizzigno P.AT3-60 Shipboard Party (2001) An off-axis hydrothermal vent field near the Mid-Atlantic Ridge at 30°N. *Nature* **412**, 145–149. http://dx.doi.org/10.1038/35084000.

Kelley D. S., Karson J. A., Früh-Green G. L., Yoerger D. R., Shank T. M., Butterfield D. A., Hayes J. M., Schrenk M. O., Olson E. J., Proskurowski G., Jakuba M., Bradley A., Larson B., Ludwig K., Glickson D., Buckman K., Bradley A. S., Brazelton W. J., Roe K., Elend M. J., Delacour A., Bernasconi S. M., Lilley M. D., Baross J. A., Summons R. E. and Sylva S. P. (2005) A serpentinite-hosted ecosystem: The Lost City hydrothermal field. *Science* **307**(5714), 1428–1434. http://dx.doi.org/10.1126/science.1102556.

Klein F., Bach W. and McCollom T. M. (2013) Compositional controls on hydrogen generation during serpentinization of ultramafic rocks. *Lithos* **178**, 55–69. http://dx.doi.org/10.1016/j.lithos.2013.03.008.

Klein F., Bach W., Humphris S. E., Kahl W.-A., Jöns N., Moskowitz B. and Berquó T. S. (2014) Magnetite in seafloor serpentinite—Some like it hot. *Geology* **42**(2), 135–138. http://dx.doi.org/10.1130/G35068.1.

Klein F., Grozeva N. G., Seewald J. S., McCollom T. M., Humphris S. E., Moskowitz B., Berquó T. S. and Kahl W.-A. (2015) Experimental constraints on fluid-rock reactions during incipient serpentinization of harzburgite. *Am. Mineral.* **100**(4), 991–1002. http://dx.doi.org/10.2138/am-2015-5112.

Kline S. R. (2006) Reduction and analysis of SANS and USANS data using IGOR Pro. *J. Appl. Crystallogr.* **39**(6), 895–900. http://dx.doi.org/10.1107/S0021889806035059.

Kong X.-Z., Tutolo B. M. and Saar M. O. (2013) DBCreate: A SUPCRT92-based program for producing EQ3/6, TOUGHREACT, and GWB thermodynamic databases at user-defined *T* and *P*. *Comput. Geosci.* **51**, 415–417. http://dx.doi.org/10.1016/j.cageo.2012.08.004.

Lafay R., Montes-Hernandez G., Janots E., Chiriac R., Findling N. and Toche F. (2012) Mineral replacement rate of olivine by chrysotile and brucite under high alkaline conditions. *J. Cryst. Growth* **347**(1), 62–72. http://dx.doi.org/10.1016/j.jcrysgro.2012.02.040.

Lang S. Q., Butterfield D. A., Schulte M., Kelley D. S. and Lilley M. D. (2010) Elevated concentrations of formate, acetate and dissolved organic carbon found at the Lost City hydrothermal field. *Geochim. Cosmochim. Acta* **74**(3), 941–952. http://dx.doi.org/10.1016/j.gca.2009.10.045.

Liu W. and Fei P. X. (2006) Methane-rich fluid inclusions from ophiolitic dunite and post-collisional mafic–ultramafic intrusion: The mantle dynamics underneath the Palaeo-Asian Ocean through to the post-collisional period. *Earth Planet. Sci. Lett.* **242**(3–4), 286–301. http://dx.doi.org/10.1016/j.epsl.2005.11.059.

Luhmann A. J., Kong X.-Z., Tutolo B. M., Ding K., Saar M. O. and Seyfried, Jr., W. E. (2013) Permeability reduction produced by grain reorganization and accumulation of exsolved CO_2 during geologic carbon sequestration: A new CO_2 trapping mechanism. *Environ. Sci. Technol.* **47**(1), 242–251. http://dx.doi.org/10.1021/es3031209.

Luhmann A. J., Kong X.-Z., Tutolo B. M., Garapati N., Bagley B. C., Saar M. O. and Seyfried, Jr., W. E. (2014) Experimental dissolution of dolomite by CO_2-charged brine at 100 °C and 150 bar: Evolution of porosity, permeability, and reactive surface area. *Chem. Geol.* **380**, 145–160. http://dx.doi.org/10.1016/j.chemgeo.2014.05.001.

Luhmann A. J., Tutolo B. M., Tan C., Moskowitz B. M., Saar M. O. and Seyfried, Jr., W. E. (2017a) Whole rock basalt alteration

from CO2-rich brine during flow-through experiments at 150 °C and 150 bar. *Chem. Geol.* **453**, 92–110. http://dx.doi.org/10.1016/j.chemgeo.2017.02.002.

Luhmann A. J., Tutolo B. M., Bagley B. C., Mildner D. F. R., Seyfried, Jr., W. E. and Saar M. O. (2017b) Permeability, porosity, and mineral surface area changes in basalt cores induced by reactive transport of CO_2-rich brine. *Water Resour. Res.* **53**(3), 1908–1927. http://dx.doi.org/10.1002/2016WR019216.

Macdonald A. H. and Fyfe W. S. (1985) Rate of serpentinization in seafloor environments. *Tectonophysics* **116**(1–2), 123–135. http://dx.doi.org/10.1016/0040-1951(85)90225-2.

Maffione M., Morris A., Plümper O. and van Hinsbergen D. J. J. (2014) Magnetic properties of variably serpentinized peridotites and their implication for the evolution of oceanic core complexes. *Geochem. Geophy. Geosy.* **15**(4), 923–944. http://dx.doi.org/10.1002/2013GC004993.

Malvoisin B., Carlut J. and Brunet F. (2012a) Serpentinization of oceanic peridotites: 1. A high-sensitivity method to monitor magnetite production in hydrothermal experiments. *J. Geophys. Res.-Sol. Ea.* **117**(B1), B01104. http://dx.doi.org/10.1029/2011JB008612.

Malvoisin B., Brunet F., Carlut J., Rouméjon S. and Cannat M. (2012b) Serpentinization of oceanic peridotites: 2. Kinetics and processes of San Carlos olivine hydrothermal alteration. *J. Geophys. Res.-Sol. Ea.* **117**, B04102. http://dx.doi.org/10.1029/2011JB008842.

Malvoisin B., Chopin C., Brunet F. and Galvez M. E. (2012c) Low-temperature wollastonite formed by carbonate reduction: a marker of serpentinite redox conditions. *J. Petrol.* **53**(1), 159–176. http://dx.doi.org/10.1093/petrology/egr060.

Marcaillou C., Muñoz M., Vidal O., Parra T. and Harfouche M. (2011) Mineralogical evidence for H_2 degassing during serpentinization at 300 °C/300 bar. *Earth Planet. Sci. Lett.* **303**(3–4), 281–290. http://dx.doi.org/10.1016/j.epsl.2011.01.006.

Martin B. and Fyfe W. S. (1970) Some experimental and theoretical observations on the kinetics of hydration reactions with particular reference to serpentinization. *Chem. Geol.* **6**, 185–202. http://dx.doi.org/10.1016/0009-2541(70)90018-5.

Mayhew L. E., Ellison E. T., McCollom T. M., Trainor T. P. and Templeton A. S. (2013) Hydrogen generation from low-temperature water-rock reactions. *Nat. Geosci.* **6**, 478–484. http://dx.doi.org/10.1038/ngeo1825.

McCollom T. M. (2016) Abiotic methane formation during experimental serpentinization of olivine. *P. Natl. Acad. Sci.* **113**(49), 13965–13970. http://dx.doi.org/10.1073/pnas.1611843113.

McCollom T. M. and Bach W. (2009) Thermodynamic constraints on hydrogen generation during serpentinization of ultramafic rocks. *Geochim. Cosmochim. Acta* **73**(3), 856–875. http://dx.doi.org/10.1016/j.gca.2008.10.032.

McCollom T. M. and Seewald J. S. (2001) A reassessment of the potential for reduction of dissolved CO_2 to hydrocarbons during serpentinization of olivine. *Geochim. Cosmochim. Acta* **65**(21), 3769–3778. http://dx.doi.org/10.1016/S0016-7037(01)00655-X.

McCollom T. M. and Seewald J. S. (2013) Serpentinites, hydrogen, and life. *Elements* **9**(2), 129–134. http://dx.doi.org/10.2113/gselements.9.2.129.

McCollom T. M., Klein F., Robbins M., Moskowitz B., Berquó T. S., Jöns N., Bach W. and Templeton A. (2016) Temperature trends for reaction rates, hydrogen generation, and partitioning of iron during experimental serpentinization of olivine. *Geochim. Cosmochim. Acta* **181**, 175–200. http://dx.doi.org/10.1016/j.gca.2016.03.002.

McDermott J. M., Seewald J. S., German C. R. and Sylva S. P. (2015) Pathways for abiotic organic synthesis at submarine hydrothermal fields. *P. Natl. Acad. Sci.* **112**(25), 7668–7672. http://dx.doi.org/10.1073/pnas.1506295112.

Mével C. (2003) Serpentinization of abyssal peridotites at mid-ocean ridges. *C. R. Geosci.* **335**(10–11), 825–852. http://dx.doi.org/10.1016/j.crte.2003.08.006.

Mildner D. F. R. and Hall P. L. (1986) Small-angle scattering from porous solids with fractal geometry. *J. Phys. D: Appl. Phys.* **19**(8), 1535–1545. http://dx.doi.org/10.1088/0022-3727/19/8/021.

Miller H. M., Mayhew L. E., Ellison E. T., Kelemen P., Kubo M. and Templeton A. S. (2017) Low temperature hydrogen production during experimental hydration of partially-serpentinized dunite. *Geochim. Cosmochim. Acta* **209**, 161–183. http://dx.doi.org/10.1016/j.gca.2017.04.022.

Miyoshi A., Kogiso T., Ishikawa N. and Mibe K. (2014) Role of silica for the progress of serpentinization reactions: Constraints from successive changes in mineralogical textures of serpentinites from Iwanaidake ultramafic body. *Japan. Am. Mineral.* **99**(5–6), 1035–1044. http://dx.doi.org/10.2138/am.2014.4748.

Moody J. B. (1976) Serpentinization: a review. *Lithos* **9**(2), 125–138. http://dx.doi.org/10.1016/0024-4937(76)90030-X.

Navarre-Sitchler A. K., Cole D. R., Rother G., Jin L., Buss H. L. and Brantley S. L. (2013) Porosity and surface area evolution during weathering of two igneous rocks. *Geochim. Cosmochim. Acta* **109**, 400–413. http://dx.doi.org/10.1016/j.gca.2013.02.012.

Navarre-Sitchler A., Brantley S. L. and Rother G. (2015) How porosity increases during incipient weathering of crystalline silicate rocks. *Rev. Mineral. Geochem.* **80**, 331–354. http://dx.doi.org/10.2138/rmg.2015.80.10.

Nesbitt H. W. and Bricker O. P. (1978) Low temperature alteration processes affecting ultramafic bodies. *Geochim. Cosmochim. Acta* **42**(4), 403–409. http://dx.doi.org/10.1016/0016-7037(78)90271-5.

Nesse W. D. (2000) *Introduction to Mineralogy*. Oxford University Press, New York.

O'Hanley D. S. (1996) *Serpentinites: Records of Tectonic and Petrological History. Oxford Monographs on Geology and Geophysics No. 34*. Oxford University Press, New York.

Okland I., Huang S., Thorseth I. H. and Pedersen R. B. (2014) Formation of H_2, CH_4 and N-species during low-temperature experimental alteration of ultramafic rocks. *Chem. Geol.* **387**, 22–34. http://dx.doi.org/10.1016/j.chemgeo.2014.08.003.

Oufi O., Cannat M. and Horen H. (2002) Magnetic properties of variably serpentinized abyssal peridotites. *J. Geophys. Res.-Sol. Ea.* **107**(B5), 2095. http://dx.doi.org/10.1029/2001JB000549.

Palandri J. L. and Reed M. H. (2004) Geochemical models of metasomatism in ultramafic systems: Serpentinization, rodingitization, and sea floor carbonate chimney precipitation. *Geochim. Cosmochim. Acta* **68**(5), 1115–1133. http://dx.doi.org/10.1016/j.gca.2003.08.006.

Plümper O., Røyne A., Magrasó A. and Jamtveit B. (2012) The interface-scale mechanism of reaction-induced fracturing during serpentinization. *Geology* **40**(12), 1103–1106. http://dx.doi.org/10.1130/G33390.1.

Pokrovsky O. S. and Schott J. (2000) Forsterite surface composition in aqueous solutions: A combined potentiometric, electrokinetic, and spectroscopic approach. *Geochim. Cosmochim. Acta* **64**(19), 3299–3312. http://dx.doi.org/10.1016/S0016-7037(00)00435-X.

Porod G. (1952) Die röntgenkleinwinkelstreuung von dichtgepackten kolloiden systemen. II Teil.. *Colloid Polym. Sci.* **125**, 51–57, and 108–122.

Proskurowski G., Lilley M. D., Seewald J. S., Früh-Green G. L., Olson E. J., Lupton J. E., Sylva S. P. and Kelley D. S. (2008) Abiogenic hydrocarbon production at Lost City hydrothermal field. *Science* **319**(5863), 604–607. http://dx.doi.org/10.1126/science.1151194.

Putnis A. (2009) Mineral replacement reactions. *Rev. Mineral. Geochem.* **70**(1), 87–124. http://dx.doi.org/10.2138/rmg.2009.70.3.

Radlinski A. P., Boreham C. J., Wignall G. D. and Lin J.-S. (1996) Microstructural evolution of source rocks during hydrocarbon generation: a small-angle-scattering study. *Phys. Rev. B* **53**(21), 14,152–14,160. http://dx.doi.org/10.1103/PhysRevB.53.14152.

Radlinski A. P., Mastalerz M., Hinde A. L., Hainbuchner M., Rauch H., Baron M., Lin J. S., Fan L. and Thiyagarajan P. (2004) Application of SAXS and SANS in evaluation of porosity, pore size distribution and surface area of coal. *Int. J. Coal Geol.* **59**(3–4), 245–271. http://dx.doi.org/10.1016/j.coal.2004.03.002.

Radlinski A. P. (2006) Small-angle neutron scattering and the microstructure of rocks. *Rev. Mineral. Geochem.* **63**(1), 363–397. http://dx.doi.org/10.2138/rmg.2006.63.14.

R Core Team (2016) *R: A Language and Environment for Statistical Computing*. R Foundation for Statistical Computing, Vienna, Austria http://www.R-project.org/.

Ruiz-Agudo E., Putnis C. V. and Putnis A. (2014) Coupled dissolution and precipitation at mineral–fluid interfaces. *Chem. Geol.* **383**, 132–146. http://dx.doi.org/10.1016/j.chemgeo.2014.06.007.

Ruiz-Agudo E., Putnis C. V., Rodriguez-Navarro C. and Putnis A. (2012) Mechanism of leached layer formation during chemical weathering of silicate minerals. *Geology* **40**(10), 947–950. http://dx.doi.org/10.1130/G33339.1.

Santelli C. M., Welch S. A., Westrich H. R. and Banfield J. F. (2001) The effect of Fe-oxidizing bacteria on Fe-silicate mineral dissolution. *Chem. Geol.* **180**(1–4), 99–115. http://dx.doi.org/10.1016/S0009-2541(01)00308-4.

Schroeder T., John B. and Frost B. R. (2002) Geologic implications of seawater circulation through peridotite exposed at slow-spreading mid-ocean ridges. *Geology* **30**(4), 367–370.

Seyfried, Jr., W. E. and Dibble, Jr., W. E. (1980) Seawater-peridotite interaction at 300 °C and 500 bars: Implications for the origin of oceanic serpentinites. *Geochim. Cosmochim. Acta* **44**(2), 309–321. http://dx.doi.org/10.1016/0016-7037(80)90139-8.

Seyfried, Jr., W. E., Foustoukos D. I. and Fu Q. (2007) Redox evolution and mass transfer during serpentinization: An experimental and theoretical study at 200 °C, 500 bar with implications for ultramafic-hosted hydrothermal systems at Mid-Ocean Ridges. *Geochim. Cosmochim. Acta* **71**(15), 3872–3886. http://dx.doi.org/10.1016/j.gca.2007.05.015.

Seyfried, Jr., W. E., Pester N. and Fu Q. (2010) Phase equilibria controls on the chemistry of vent fluids from hydrothermal systems on slow spreading ridges: Reactivity of plagioclase and olivine solid solutions and the pH-silica connection. In *Diversity of Hydrothermal Systems on Slow Spreading Ocean Ridges, Geophysical Monograph Series 188* (eds. P. A. Rona, C. W. Devey, J. Dyment and B. J. Murton). American Geophysical Union, Washington, DC, pp. 297–320.

Seyfried, Jr., W. E., Pester N. J., Tutolo B. M. and Ding K. (2015) The Lost City hydrothermal system: Constraints imposed by vent fluid chemistry and reaction path models on subseafloor heat and mass transfer processes. *Geochim. Cosmochim. Acta* **163**, 59–79. http://dx.doi.org/10.1016/j.gca.2015.04.040.

Sharp Z. D. and Barnes J. D. (2004) Water-soluble chlorides in massive seafloor serpentinites: A source of chloride in subduction zones. *Earth Planet. Sc. Lett.* **226**(1–2), 243–254. http://dx.doi.org/10.1016/j.epsl.2004.06.016.

Streit E., Kelemen P. and Eiler J. (2012) Coexisting serpentine and quartz from carbonate-bearing serpentinized peridotite in the Samail Ophiolite, Oman. *Contrib. Mineral. Petr.* **164**(5), 821–837. http://dx.doi.org/10.1007/s00410-012-0775-z.

Stumm W. and Morgan J. J. (1996) *Aquatic Chemistry: Chemical Equilibria and Rates in Natural Waters*, third ed. John Wiley & Sons, New York.

Tingle T. N. and Hochella, Jr., M. F. (1993) Formation of reduced carbonaceous matter in basalts and xenoliths: Reaction of C-O-H gases on olivine crack surfaces. *Geochim. Cosmochim. Acta* **57**(14), 3245–3249. http://dx.doi.org/10.1016/0016-7037(93)90537-7.

Tingle T. N., Hochella, Jr., M. F., Becker C. H. and Malhotra R. (1990) Organic compounds on crack surfaces in olivine from San Carlos, Arizona and Hualalai Volcano, Hawaii. *Geochim. Cosmochim. Acta* **54**(2), 477–485. http://dx.doi.org/10.1016/0016-7037(90)90337-K.

Tingle T. N., Mathez E. A. and Hochella, Jr., M. F. (1991) Carbonaceous matter in peridotites and basalts studied by XPS, SALI, and LEED. *Geochim. Cosmochim. Acta* **55**(5), 1345–1352. http://dx.doi.org/10.1016/0016-7037(91)90312-S.

Toft P. B., Arkani-Hamed J. and Haggerty S. E. (1990) The effects of serpentinization on density and magnetic susceptibility: a petrophysical model. *Phys. Earth Planet. In.* **65**(1–2), 137–157. http://dx.doi.org/10.1016/0031-9201(90)90082-9.

Tutolo B. M., Luhmann A. J., Kong X.-Z., Saar M. O. and Seyfried, Jr., W. E. (2014) Experimental observation of permeability changes in dolomite at CO_2 sequestration conditions. *Environ. Sci. Technol.* **48**(4), 2445–2452. http://dx.doi.org/10.1021/es4036946.

Tutolo B. M., Luhmann A. J., Kong X.-Z., Saar M. O. and Seyfried, Jr., W. E. (2015) CO_2 sequestration in feldspar-rich sandstone: Coupled evolution of fluid chemistry, mineral reaction rates, and hydrogeochemical properties. *Geochim. Cosmochim. Acta* **160**, 132–154. http://dx.doi.org/10.1016/j.gca.2015.04.002.

Tutolo B. M., Mildner D. F. R., Gagnon C. V. L., Saar M. O. and Seyfried, Jr., W. E. (2016) Nanoscale constraints on porosity generation and fluid flow during serpentinization. *Geology* **44**(2), 103–106. http://dx.doi.org/10.1130/G37349.1.

Wang D. T., Reeves E. P., Seewald J. S., McDermott J. M. and Ono S. (2016) Clumped isotopologue constraints on the origin of methane in basalt- and ultramafic-hosted mid-ocean ridge hydrothermal fluids. Goldschmidt Conference Abstracts, pp. 3310.

Wark D. A., Williams C. A., Watson E. B. and Price J. D. (2003) Reassessment of pore shapes in microstructurally equilibrated rocks, with implications for permeability of the upper mantle. *J. Geophys. Res.-Sol. Ea.* **108**(B1), 2050. http://dx.doi.org/10.1029/2001JB001575.

Warton D. I., Wright I. J., Falster D. S. and Westoby M. (2006) Bivariate line-fitting methods for allometry. *Biol. Rev.* **81**(2), 259–291. http://dx.doi.org/10.1017/S1464793106007007.

Warton D. I., Duursma R. A., Falster D. S. and Taskinen S. (2012) SMATR 3–An R package for estimation and inference about allometric lines. *Methods Ecol. Evol.* **3**(2), 257–259. http://dx.doi.org/10.1111/j.2041-210X.2011.00153.x.

Wegner W. W. and Ernst W. G. (1983) Experimentally determined hydration and dehydration reaction rates in the system MgO-SiO2-H2O. *Am. J. Sci.* **283-A**, 151–180.

White A. F. and Peterson M. L. (1990) Role of reactive-surface-area characterization in geochemical kinetic models. In *Chemical Modeling of Aqueous Systems II* (eds. D. C. Melchoir and R. L. Bassett). American Chemical Society, pp. 461–475 (Chap. 35).

Wilke M., Farges F., Petit P.-E., Brown, Jr., G. E. and Martin F. (2001) Oxidation state and coordination of Fe in minerals: An Fe K-XANES spectroscopic study. *Am. Mineral.* **86**(5–6), 714–730. http://dx.doi.org/10.2138/am-2001-5-612.

Wogelius R. A. and Walther J. V. (1992) Olivine dissolution kinetics at near-surface conditions. *Chem. Geol.* **97**(1–2), 101–112. http://dx.doi.org/10.1016/0009-2541(92)90138-U.

Associate Editor: Wolfgang Bach